Ore Geology Reviews 139 (2021) 104533

Contents lists available at ScienceDirect

Ore Geology Reviews

journal homepage: www.elsevier.com/locate/oregeorev

In situ multiple sulfur isotopes and chemistry of pyrite support a sedimentary source-rock model for the Linwang Carlin-type gold deposit in the Youjiang basin, southwest China

Xinghua He [a,b], Wenchao Su [a,*], Nengping Shen [a], Xiaoping Xia [c], Fangyue Wang [d]

[a] State Key Laboratory of Ore Deposit Geochemistry, Institute of Geochemistry, Chinese Academy of Sciences, Guiyang 550081, China
[b] University of Chinese Academy of Sciences, Beijing 100049, China
[c] State Key Laboratory of Isotope Geochemistry, Guangzhou Institute of Geochemistry, Chinese Academy of Sciences, Guangzhou 510640, China
[d] Ore Deposit and Exploration Centre, Hefei University of Technology, Hefei 230009, China

ARTICLE INFO

Keywords:
Pyrite
In situ multiple sulfur isotopes
Trace elements
Linwang Carlin-type gold deposit
Youjiang basin
China

ABSTRACT

The Linwang gold deposit is a representative example of Carlin-type gold deposits in Youjiang basin, southwest China. High-grade ores are hosted in silicified and brecciated siltstone, sandstone, and mudstone of the Middle Triassic and are controlled by high-angle reverse faults. Optical microscopy pyrite texture, in situ laser ablation-inductively coupled mass spectrometry (LA-ICP-MS) trace elements, and secondary ion mass spectrometry (SIMS) multiple sulfur isotopes analyses are used to examine the different types of pyrites to constrain the sources of reduced sulfur and metals for the Linwang deposit.

Petrography and pyrite chemistry studies distinguished three generations of pyrite: Pre-ore pyrite (Py 1) and ore pyrites (Py 2 and Py3). Pre-ore pyrite is framboidal, anhedral to euhedral pyrite with highest concentrations of Co, Ni, and Pb and is interpreted to have a sedimentary (diagenetic) origin. Ore pyrites were formed by hydrothermal fluids via sulfidation of Fe-bearing minerals in the host rocks. They commonly rimed and partially replaced the pre-ore pyrite and have an As-rich inner rim (Py 2) and an Au-rich outer rim (Py 3) with lowest contents of Co, Ni, and Pb. All pyrites contain Au, As, Sb, Cu, Tl, and Se, with increasing concentrations from Py 1 to Py 3.

In situ SIMS multiple S isotope analyses show that all pyrites in the Linwang deposit have narrow ranges of $\delta^{34}S$ values, with average of +5.13‰ for Py 1, +4.84‰ for Py 2, and +4.53‰ for Py 3, and near zero of $\Delta^{33}S$ values (−0.02‰ to +0.03‰), suggesting that the S within the Linwang deposit was most likely sourced from the Triassic sedimentary rocks that host the deposit. A near zero $\Delta^{33}S$ signature in all pyrites indicates no record of the assimilation of Archean sulfur, implying the deep basement of Archean rocks beneath the basin were not involved the formation of the Linwang deposit.

Oxygen and hydrogen isotope compositions of ore fluids ($\delta^{18}O_{H2O}$ = +11.7‰ to +16.5‰, δD = −71‰ to −57‰) indicate a metamorphic origin. Based on these data, we propose a sedimentary source-rock model for the Linwang deposit in which the ore fluids were generated by release of previous Au-bearing sedimentary pyrites during metamorphism of sedimentary rocks. The stress relaxation of Yanshanian orogeny resulted in the ore fluids flowed upward along the fault zones into structural highs where they reacted with Fe-bearing minerals in the host rocks to deposit Au-rich pyrite. The preconcentration of Au, As, and Sb in sedimentary pyrite and gold deposition process are key to the formation of the Linwang deposit and may apply to the genesis of other Carlin-type gold deposits in the Youjiang basin.

1. Introduction

Carlin-type gold deposits are well-known in Nevada, USA, and the Youjiang basin, Southwest China, which are endowed with approximately 8000 and 800 tons of gold, respectively, making them the most important metallogenic provinces for Carlin-type gold deposits in the world (Muntean and Cline, 2018; Su et al., 2018). These deposits are mainly hosted in impure carbonate or calcareous and carbonaceous

* Corresponding author.
E-mail address: suwenchao@vip.gyig.ac.cn (W. Su).

https://doi.org/10.1016/j.oregeorev.2021.104533
Received 10 September 2021; Received in revised form 18 October 2021; Accepted 18 October 2021
Available online 24 October 2021

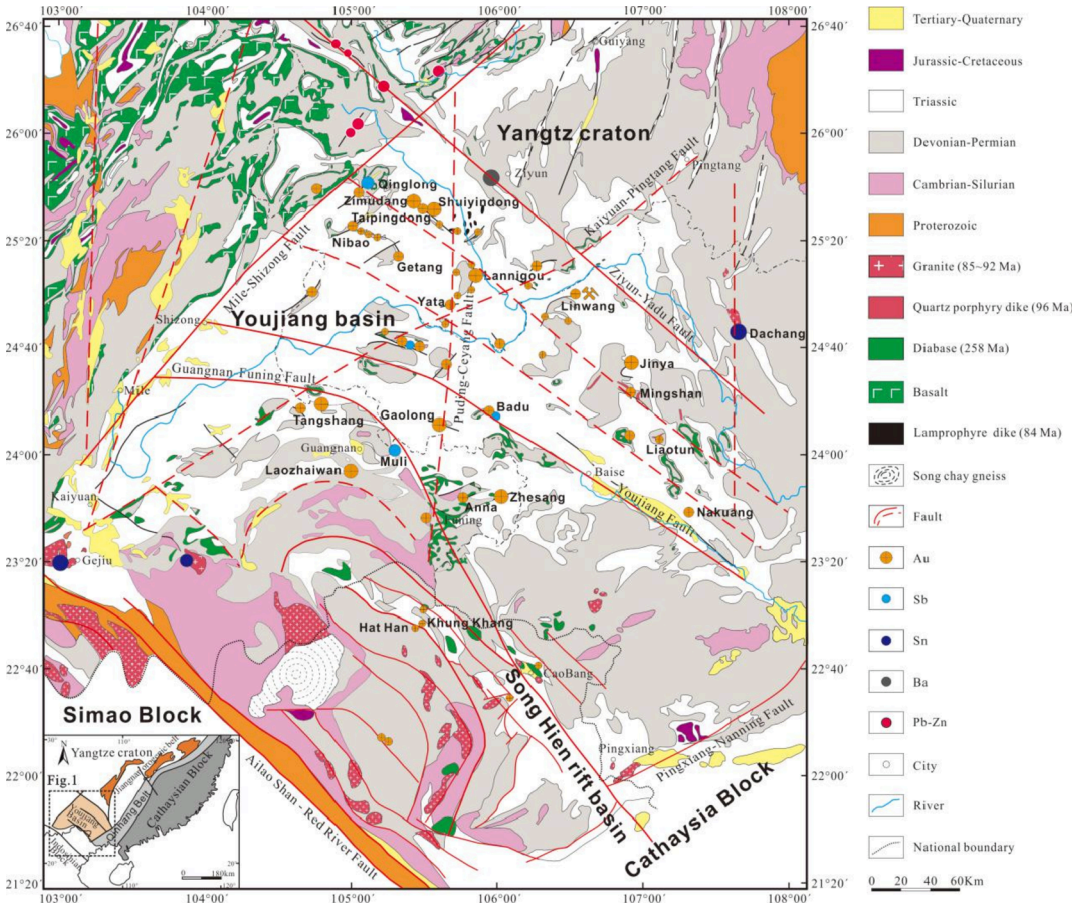

Fig. 1. Geological map of the Youjiang basin and distribution of Carlin-type gold and other deposits in China and in northern Vietnam (modified from Su et al., 2018).

sedimentary rocks and are characterized by decarbonatization, silicification, sulfidation, and argillization (Hofstra and Cline, 2000; Cline et al., 2005; Cline 2018; Kesler et al., 2005; Muntean and Cline, 2018; Su et al., 2008, 2009a, b, 2012, 2018). Gold occurs mainly as invisible forms of structurally bounded Au^{1+} and/or nanoparticles in arsenian pyrite (Simon et al., 1999; Palenik et al., 2004; Reich et al., 2005; Gopon et al., 2019; Su et al., 2008, 2012; Liang et al., 2020).

The process of Carlin-type ore formation is well understood. Sulfidation is recognized to be the most important mechanism of gold deposition, whereby gold and pyrite precipitated together from H_2S-rich, Fe-poor fluids that reacted with Fe-bearing minerals in the host-rock package (Hofstra et al., 1991; Hofstra and Cline, 2000; Kesler et al., 2003; Cline et al., 2005; Cline 2018; Muntean and Cline, 2018; Su et al., 2009a, 2018; Kusebauch et al., 2019). Genetic model previously proposed for Carlin-type gold deposits in Nevada and Youjiang basin falls into three groups involving magmatic (Ressel et al., 2000; Cline et al., 2005; Hou et al., 2016; Cline 2018; Muntean and Cline, 2018; Xie et al., 2018a, b; Zhu et al., 2019), metamorphic (Groves et al., 1998; Hofstra and Cline, 2000; Su et al., 2009a, 2018; Li et al., 2020; Lin et al., 2021), and circulated meteoric waters (Ilchik and Barton, 1997; Hu et al., 2002; Emsbo et al., 2003) or basin brines (Gu et al., 2012). These models are mainly based on interpretations of sulfur isotope compositions of sulfides.

However, the sulfur isotope compositions of ore pyrites in Nevada and Youjiang basin varied significantly within and between mining districts. For example, In Nevada, the $\delta^{34}S$ value of ore pyrite from the high-grade Meikle deposit in the northern Carlin trend and the Jerritt Canyon district is about +10‰ (Emsbo et al., 2003; Cline et al., 2005), whereas in the Getchell trend and Screamer section on the margin of Betze-Post deposit, the $\delta^{34}S$ value of ore pyrite is near zero (Kesler et al., 2005; Hofstra et al., 2011). In Youjiang basin, in-situ sulfur isotope analyses of ore pyrites from a cluster of carbonate-hosted gold deposits on the platform of the basin, including Shuiyindong, Taipingdong, Nibao, and Getang deposits, yielded a near zero of $\delta^{34}S$ value (Hou et al., 2016; Hu et al., 2018; Xie et al., 2018b; Li et al., 2020; Liang et al., 2020; Zhao et al., 2020; Wei et al., 2020; Lin et al., 2021), whereas the ore pyrites from siliciclastic-hosted gold deposits in the basin such as Lannigou, Yata, Jinya, and Gaolong deposits have a large variation of $\delta^{34}S$ value (−4.5‰ to +18.1‰) (Su et al., 2018; Yan et al., 2018; Xie et al., 2018a, b; Lin et al., 2021). These ambiguous results led to interpretations for S isotope compositions either magmatic or sedimentary source or mixing of them (Muntean et al., 2011; Hou et al., 2016; Su et al., 2018; Xie et al., 2018a, Xie et al., 2018b).

The development of laser ablation-multicollector-inductively coupled plasma-mass spectrometry (LA-MC-ICP-MS), sensitive high-resolution ion microprobe (SHRIMP), and secondary ion mass spectrometry (SIMS) allow in situ analyses to distinguish trace elements and S isotope compositions between pre-ore and ore pyrites (Kesler et al., 2005; Large et al., 2007, 2009; Barker et al., 2009; Hou et al., 2016; Xie et al., 2018a, b; Yan et al., 2018; Lin et al., 2021). In this study, we first use LA-ICP-MS and SIMS to determine trace element compositions and multiple sulfur isotopes (^{32}S, ^{33}S, and ^{34}S) for pre-ore and ore pyrites from the Linwang Carlin-type gold deposit in the Youjiang basin, southwest China, to constrain the sources of reduced sulfur and metals. For comparison, we compiled in-situ $\delta^{34}S$ data from the literatures for pre-ore and ore pyrites and in-situ Au, As, and Sb contents of sedimentary pyrites from other Carlin-type gold deposits in the Youjiang basin. All data support a sedimentary source-rock of sulfur and metals and

Table 1
Isotope dating ages of Carlin-type gold deposits in the Youjiang basin, China and Northern Vietnam.

Deposit	Location	Age/Method	References
Nibao	Northern Youjiang basin	141 ± 3 Ma/Ap Th-Pb	Chen et al., 2019
Shuiyindong	Northern Youjiang basin	134 ± 3 Ma/Cal Sm-Nd	Su et al., 2009b
		144 ± 19 Ma/Cal U-Pb	Huang, 2019
Lannigou	Northern Youjiang basin	128 ± 4.6 Ma/Cal U-Pb	Huang, 2019
Yata	Northern Youjiang basin	144 ± 12 Ma/Ap U-Pb	Huang, 2019
Jinya	Northern Youjiang basin	146.1 ± 4.2 Ma/Ap U-Pb	Gao, 2018
Badu	Northern Youjiang basin	141.7 ± 5.8 Ma/Rut U-Pb	Gao et al., 2021
		143.5 ± 1.4 Ma/Mnz Th-Pb	
Gaolong	Southern Youjiang basin	209 ± 26 Ma/Bit Re-Os	Jin, 2017
Zhesang	Southern Youjiang basin	213.6 ± 5.4 Ma/Rut U-Pb	Pi et al., 2017
		215.3 ± 1.9 Ma/Ill Ar-Ar	
		212 ± 9 Ma/Py Rb-Sr	Dong, 2017
Laozhaiwan	Southern Youjiang basin	207.9 ± 5.9 Ma, 216.9 ± 3.4 Ma, 223.9 ± 6.9 Ma/Mnz U-Pb	Hu et al., 2017
Anna	Southern Youjiang basin	232 ± 5 Ma/ill Ar-Ar	Dong, 2017
Hat Han	Southern Youjiang basin, northern Vietnam	209.1 ± 2.3 Ma/Ser Ar-Ar	Nevolko et al., 2017
Khung Khoang	Southern Youjiang basin, northern Vietnam	211.6 ± 2.3 Ma/Ser Ar-Ar	Nevolko et al., 2017

Abbreviations: Ap = apatite, Cal = calcite, Rut = rutile, Mnz = monazite, Ill = illite, Py = pyrite, Bit = bitumen, Ser = sericite.

metamorphic ore fluids for Carlin-type gold mineralization in the Youjiang basin, southwest China.

2. Regional geology

Carlin-type gold deposits in the southwestern China are restricted to the Youjiang basin (Fig. 1), which is bound by the Mile-Shizong fault to the northwest, by the Ziyun-Yadu fault to the northeast, and by the Pingxiang-Nanning fault to the southeast, which separates the basin from the Cathaysia block (Su et al., 2018). The southern edge of the Youjiang basin is dominated by metamorphic rocks of the North Vietnam terrane, which is separated from the Simao block by the Ailao Shan-Red River shear zone (Du et al., 2013; Hou et al., 2016).

The Youjiang basin (Fig. 1) was produced by Devonian rifting of the southwest margin of the Yangtze craton (Su et al., 2018) and has experienced successive development of passive continental margin rift basin (Early Devonian to early Permian), back-arc basin (Late Permian to Early Triassic), and foreland basin (Middle to Late Triassic) related to the opening, subduction and closing of the Paleo-Tethys ocean (Yang et al., 2012; Du et al., 2013; Yang et al., 2020; Lin et al., 2021). The basin consists of Precambrian to Ordovician basement and a cover sequence of Devonian to Triassic sedimentary rocks (Yang et al., 2020). The oldest basement rock is composed of ca. 799 Ma gneiss (zircon U-Pb dating; Yan et al., 2006) exposed in the Song Chay in the southern part of the Youjiang basin (Yang et al., 2020). A cover sequence of Devonian to Triassic sedimentary rocks is recorded throughout the basin. The Devonian strata mainly crops out in the southwestern part of the basin and consist of sandstone, siltstone, and shale that unconformably overlie Cambrian-Ordovician calcareous rocks and shale (Du et al., 2013; Hou et al., 2016). The Permian limestone and Triassic siltstone, sandstone, and mudstone are widely distributed throughout the basin (Fig. 1), with Permian rocks generally exposed in the cores of anticlines. Most of sedimentary rocks in the basin underwent low-grade burial metamorphism as recorded by illite crystallinites (Suo et al., 1998).

The basin sequences were deformed by two subduction-related tectonic events. In the southeastern part of the basin, W-verging subduction of the Pacific plate beneath the Eurasian plate during the Middle Permian caused NE-striking folding and faulting of the basin sequences and intensive felsic magmatism along the eastern margin of China (Li and Li, 2007), far from the Carlin-type gold deposits. In the southwestern part of the basin, NE-verging subduction of the Ailaoshan-Song Ma branch of the Paleo-Tethys ocean beneath the Indochina block during the Early Permian and controlled the evolution of the Youjiang basin (Lai et al., 2014; Zaw et al., 2014). Continued subduction eventually brought about the Indochina-South China collision (Indosinian orogeny) during the Late Permian to Middle Triassic (Zaw et al., 2014). Following the Late Triassic-Early Jurassic Indochina-Sibumasu collision (Yanshanian orogeny) and Cretaceous subduction of the Meso-Tethys oceanic plate beneath Sibumasu (Cai and Zhang, 2009; Zaw et al., 2014) led to intracontinental deformation and extension of the Youjiang basin, respectively. Extension may have caused emplacement of the Cretaceous quartz porphyry dikes (96 Ma: Chen et al., 2014; Zhu et al., 2017) and lamprophyre dikes (88 Ma: Su, 2002; Liu et al., 2010) in the Youjiang basin. Su et al. (2018) suggested that the two compressional events contributed to formation of Middle-Late Triassic (232–212 Ma) gold deposits on the southern margin (e.g., Anna, Zhesang, and Laozhaiwan, Table 1) and the Late Jurassic-Early Cretaceous (148–134 Ma) gold deposits on the northern margin of the Youjiang basin (e.g., Shuiyindong, Lannigou, and Nibao), which is divided by the Youjiang fault (Fig. 1).

Carlin-type gold deposits in the Youjiang basin occur in clusters around a series of NW-and NE-striking extensional faults (Fig. 1). The largest deposits are strata-bound and are hosted in Permian bioclastic limestone interbedded with calcareous siltstone and sandstone on the northern margin of the basin (e.g., Shuiyindong). Others are fault-controlled and occur along high-angle reverse faults and adjacent altered rocks in the basin, with ore hosted in the Triassic calcareous siltstone, sandstone, and mudstone (e.g., Lannigou). Smaller deposits occur in Cambrian to Triassic siliciclastic rocks and locally in Late Permian diabase intrusions on the southern margin of the basin (e.g., Anna). Although the ore controls vary, these deposits have many characteristics in common with Carlin-type gold deposits in Nevada, including lithology of host rocks, mineral assemblages, alteration types, elemental associations, and occurrence of gold (Su et al., 2018; Xie et al., 2018a).

3. Geology of the Linwang deposit

The Linwang deposit is located at the northern part of the Youjiang basin (Fig. 1). It lies on the northeastern flank of Leye isolated carbonate platform (Fig. 2) and occurs along high-angle reverse faults and adjacent altered rocks, with ore hosted in calcareous siltstone, sandstone, and mudstone of the Middle Triassic Banna and Baifeng Formations. Recent exploration and mining at the Linwang have proven gold reserves of 30 metric tons (t) Au (Gao, 2018), with average gold grades of 4 g/t (Chen et al., 2010).

Sedimentary rocks in the district consist of the Middle Permian limestone and the Lower-Middle Triassic siltstone, sandstone, and mudstone (Fig. 2). The Middle Permian Heshan Formation, a massive

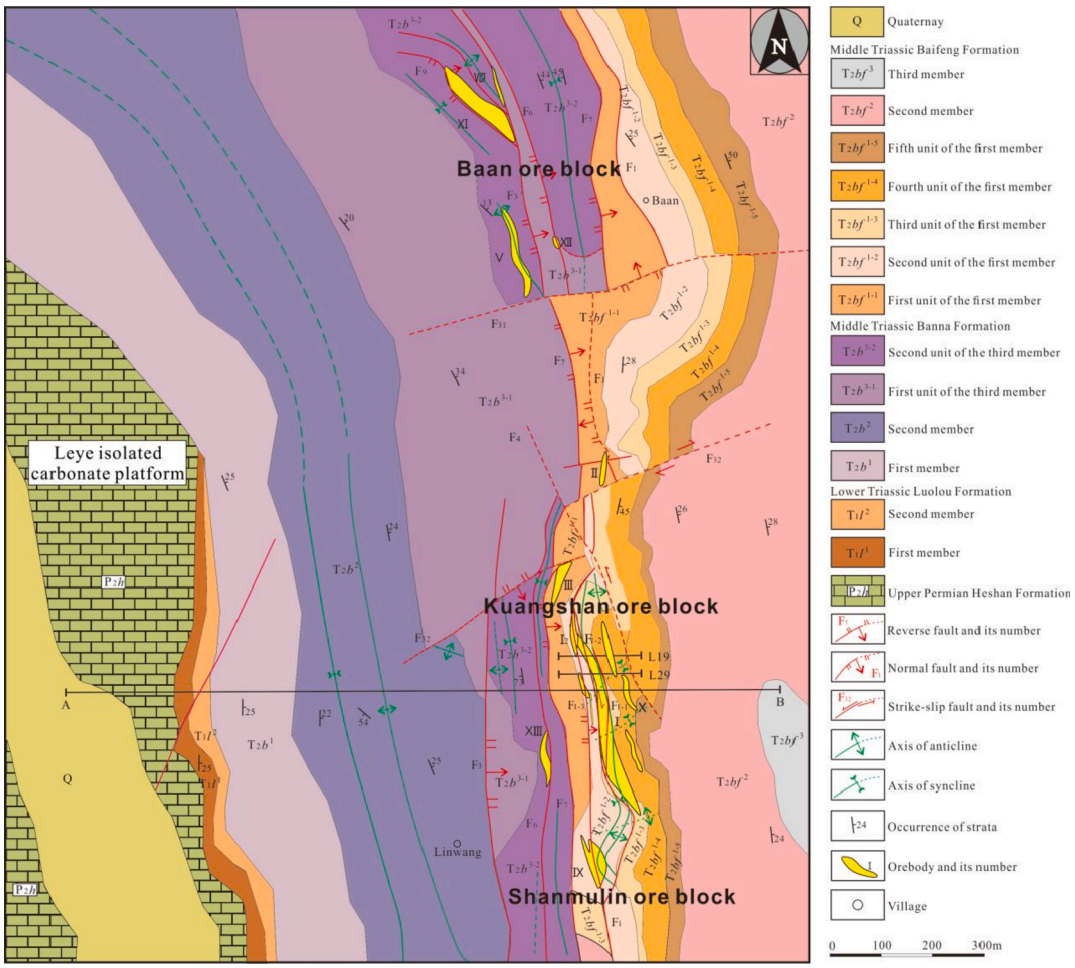

Fig. 2. Geological plan of the Linwang deposit in the Youjiang basin (modified from Chen et al., 2010).

limestone, is overlain by the Lower Triassic Luolou Formation and the Middle Triassic Banna and Baifeng Formations. The Lower Triassic Luolou Formation consists of limestone and mudstone interbedded with limestone. The Middle Triassic Banna and Baifeng Formations are dominated by sandstone, siltstone, and mudstone, which are divided into three members based on sand grain size and bedding thickness, respectively (Chen et al., 2010). Gold mineralization is mainly hosted in the second unit of the third member of the Banna Formation and the first and second units of the first member of the Baifeng Formation (Figs. 2 and 3), which are composed of siltstone and sandstone interbedded with mudstone. No coeval felsic intrusive rocks to date were observed in the vicinity of the Linwang deposits, with an exception at the Liaotun gold deposit where a 96 Ma quartz porphyry dike crosscuts the gold orebody (Fig. 1; Chen et al., 2014).

Gold mineralization (Figs. 2 and 3) occurs along a narrow N-S trending zone and comprises more than 10 orebodies (Chen et al., 2010). Most of them occur along high-angle and strike-slip faults that cut the east flank of the Leye anticline. The flank of the anticline dips at 20° to 25°, locally containing chevron folds and mesoscopic compressive fracture zones. The largest orebody (I) is controlled by the F_1 and $F_{1\text{-}2}$ fault zones (Fig. 3) and contains ~ 65% of gold reserves at the Linwang (Chen et al., 2010), with ore hosted in the Middle Triassic Baifeng Formation. The mineralization zone is 600 m long, 30 to 90 m wide, and 40 to 160 m thick, with average of gold grade of 4 g/t. Some orebodies occur as lens-shaped, veins, and vein stockworks within the Middle Triassic Banna Formation and are structurally controlled by secondary faults (Fig. 2). High-grade ore samples (7.33 g/t to 21.6 g/t Au) used in this study collected from the orebody (I) are characterized by a dense distribution of disseminated sulfides in silicified and brecciated siltstone, along with abundant barren milky quartz and calcite veinlets (Fig. 4).

Wall-rock alteration identified in this study includes decarbonatization, silicification, sulfidation, argillization (illite), and dolomitization, similar to those of the siliciclastic-hosted gold deposits in the Youjiang basin such as the Lannigou and Yata deposits (Su et al., 2009a; Xie et al., 2018a). Sulfides in the deposit consist mainly of arsenian pyrite, minor arsenopyrite and stibnite (Chen et al., 2010). Arsenian pyrite is the main host mineral for invisible gold (Gao et al., 2021).

The mineral paragenesis (Fig. 6) includes pre-ore minerals such as ferroan calcite and dolomite, detrital quartz, trace muscovite, apatite, rutile, kaolinite and disseminated pyrite that were likely incorporated into the host rocks during sedimentation and/or diagenesis. Ore-related minerals are divided into two stages according to crosscutting relations and mineral assemblages. The ore stage minerals consist of barren quartz veinlets, arsenian pyrite, illite, and dolomite. The quartz veinlets are spatially associated with higher-grade ores, and arsenian pyrites are disseminated into the host rocks around quartz veinlets (Fig. 5m), we infer that the quartz veinlets are ore related. The late ore stage minerals are dominated by stibnite, vein quartz, calcite and dolomite, which commonly fill fractures and locally cement brecciated siltstone.

4. Samples and analytical methods

Seven samples (Fig. 4) used in this study were collected from the largest orebody (I) at the open-pit of the Linwang deposit (Fig. 3). A total of 26 polished sections were prepared and examined using transmitted

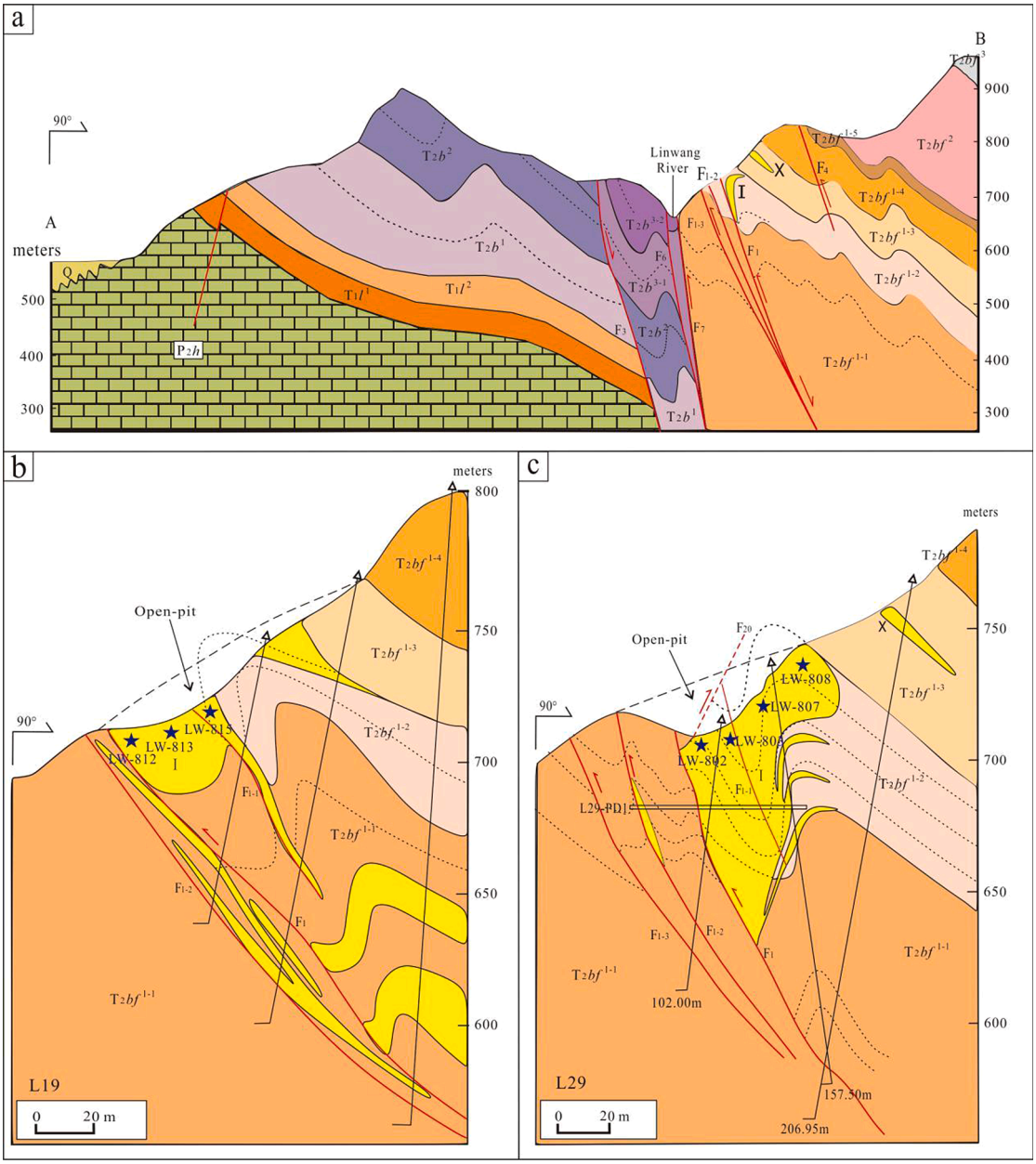

Fig. 3. Cross-sections of A-B (a), L19 (b), and L29 (c) and sample locations of the Linwang deposit. The cross-section locations and legends showing on the Fig. 2 (modified from Chen et al., 2010).

and reflected light microscopy to identify minerals and to observe morphology and texture. Sulfides and other minerals were further identified using a JXA8230 electron microprobe at the State Key Laboratory of Ore Deposit Geochemistry (SKLODG), Institute of Geochemistry, Chinese Academy of Sciences, Guiyang, China. High-resolution images were obtained using a JSM-7800F scanning electron microscope (SEM) at the SKLODG, to illustrate the morphology and texture of pyrite, and provide precise locations for LA-ICP-MS and SIMS analyses.

4.1. *In situ trace element analysis of pyrite*

In situ trace element analyses of pyrites from 7 polished sections were conducted using LA-ICP-MS at the In-situ Mineral Microanalysis Laboratory of the Ore Deposit and Exploration Centre (ODEC), Hefei University of Technology, China. The analyses were carried out on an Agilent 7900 Quadrupole ICP-MS coupled to a Photon Machines Analyte HE 193-nm ArF Excimer laser ablation system. The procedure and operation conditions were described in detail by Wang et al. (2017) and Du et al., (2021), which are summarized below.

The sample was ablated in an atmosphere of ultra-high purity He, which was used as a carrier gas (0.9 L/min.), and the resulting aerosol was mixed with Ar (0.87 L/min.) prior to introduction into the mass spectrometer. Ablation was performed using an energy density of 2 J/cm^2 and a laser pulse frequency of 8 Hz. The laser spot size used in this study is 20 μm. The total acquisition time for each spot analysis was 60 s, consisting of a 20 s background measurement with the laser turned off and 40 s peak signal measurement with the laser turned on. A 30 s delay was instituted after each individual spot analysis to ensure that the ablation cell was effectively washed out and the gases had stabilized. During the spot analysis and mapping, the following isotopes were monitored: ^{34}S, ^{57}Fe, ^{59}Co, ^{60}Ni, ^{63}Cu, ^{66}Zn, ^{75}As, ^{107}Ag, ^{121}Sb, ^{197}Au, ^{201}Hg, ^{205}Tl, ^{208}Pb, and ^{209}Bi.

Mapping of pyrite was performed by ablating sets of parallel lines in a grid across the samples. Depending on the sample size, lines were

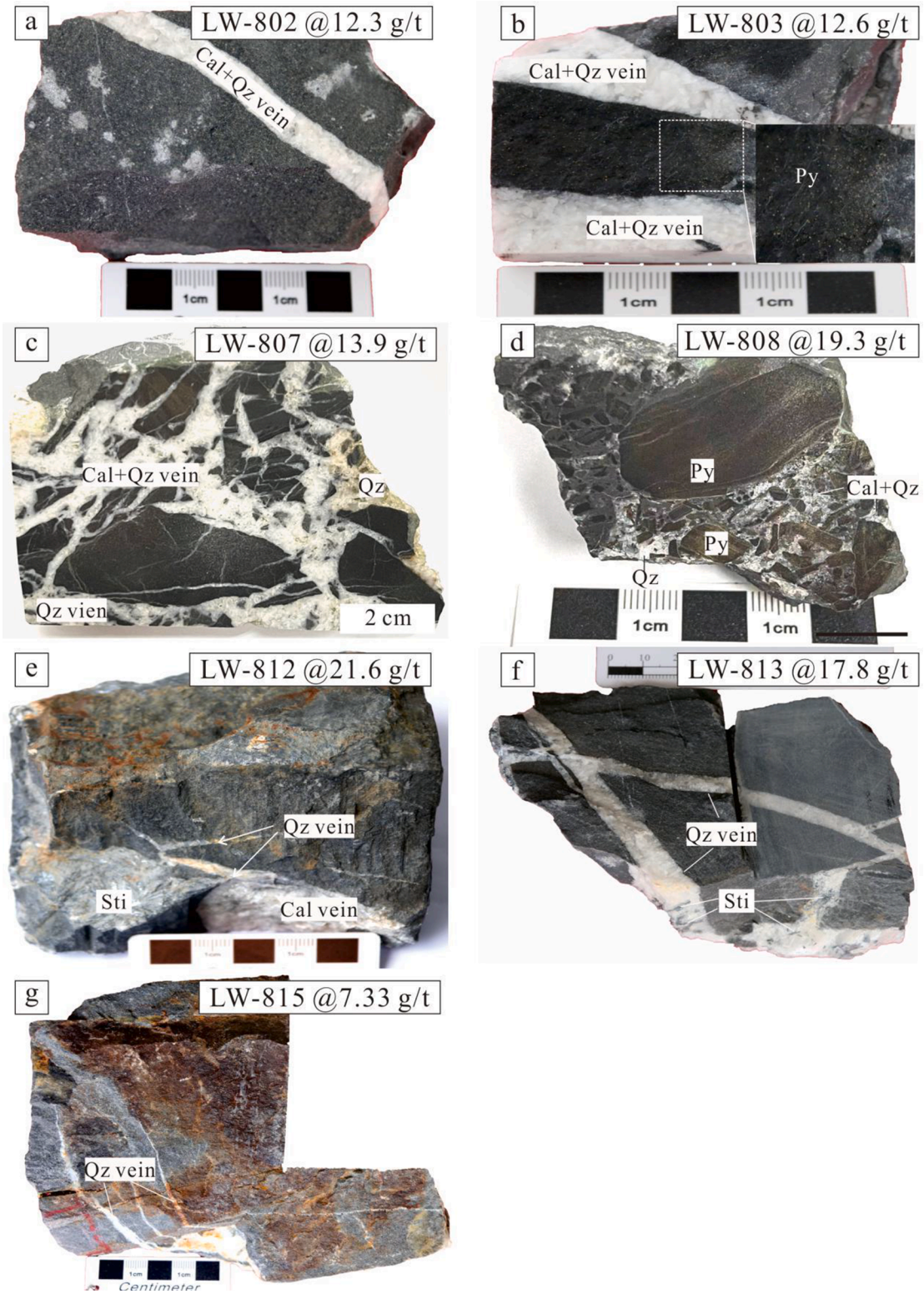

Fig. 4. Photograph of samples used in this study from the Linwang deposit. Abbreviations: Cal = calcite, Qz = quartz, Py = pyrite, Sti = stibnite.

ablated with a beam size of 10 or 20 μm. The spacing between the lines was kept constant at the same size as the laser beam. The laser beam scan speed for each line was equal to the beam size per second. LA-ICP-MS trace element maps were generated over a period of 1.5 to 2 h to keep the sensitivity of the instrument drift to a minimum.

The off-line data processing was performed using a program called ICPMSDataCal (Liu et al., 2008). Trace element compositions of samples were calibrated against multiple-references materials with applying iron as the internal normalization element. Analytical errors for trace elements in sulfides are less than 30% according to MASS-1 (Feng and Li, 2019). Images were compiled and processed using the laboratory software LIMS (designed based on Matlab, Wang et al., 2017). Analyses of the Linwang pyrite were calibrated using NIST610 glass and the MASS-1 synthetic sulfide reference material (Wilson et al., 2002).

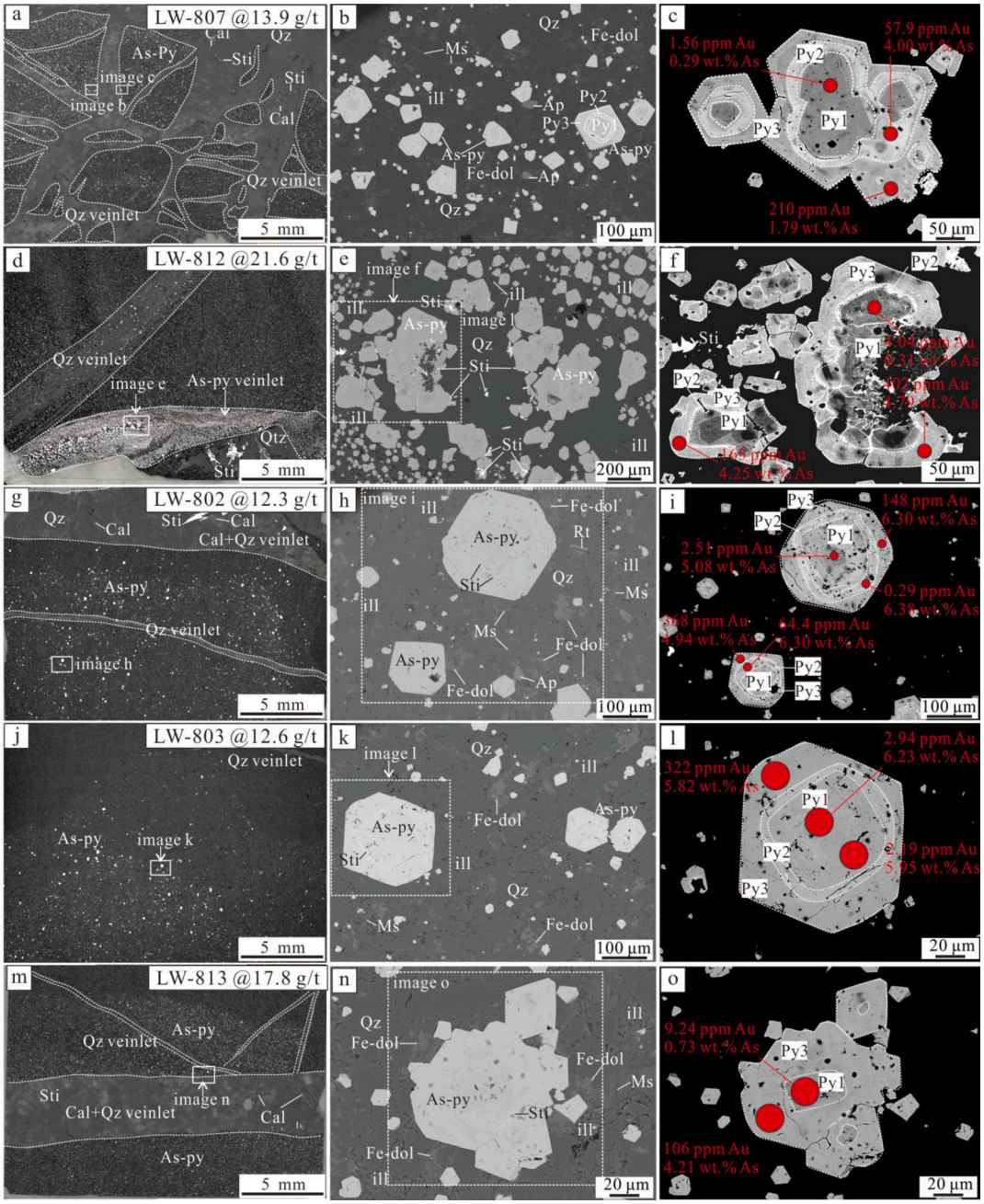

Fig. 5. Images of polished sections for each sample on the left, SEM or electron microprobe BSE images of selected area in the middle, and pyrite type and texture on the right. Red dots indicate locations of LA-ICP-MS analyses, with Au and As concentrations. Abbreviations: As-Py = arsenian pyrite, Fe-dol = Fe dolomite, ill = illite, Cal = calcite, Qz = quartz, Sti = stibnite, Ms = muscovite, Ap = apatite, Rt = rutile, Py1 = pre-ore pyrite 1, Py2 = ore pyrite 2 (inner rim), Py3 = ore pyrite 3 (outer rim). (For interpretation of the references to color in this figure legend, the reader is referred to the web version of this article.)

4.2. *In situ S isotope analysis of pyrite*

Two representative polished sections (LW-808 and LW-815) from the Linwang deposit were selected for the in situ SIMS S isotope analyses after LA-ICP-MS trace element analyses. Pyrites were sampled using a microdrill and cast in epoxy mounts. The epoxy mounts were carefully polished with diamond paste and coated by a gold layer with a thickness of about 30 nm before SIMS analysis. The standards used in this study were PPP-1 (Gilbert et al., 2014) for pyrite. The SIMS measurements were conducted at the Guangzhou Institute of Geochemistry, Chinese Academy of Sciences (GIGCAS), using a CAMECA IMS 1280-HR instrument. The analytical parameters were similar to those described in Li et al. (2018) and are briefly summarized here: A primary beam of $^{133}Cs^{+}$ ion (~2.0 nA current and 20 keV total impact energy) was focused on the sample surface with a spot diameter of 20 μm. A 15 μm raster was applied during all analyses to slightly homogenize the Gaussian beam. Presputtering for 20 s was applied to remove the Au coating, and a normal-incidence electron gun was used for charge compensation. The mass resolving power was set at 5000 to avoid isobaric interferences. A NMR field sensor was applied to stabilize the magnetic field. ^{32}S, ^{33}S and ^{34}S were measured simultaneously by three Faraday cups of the multi-collection system (L2, L1 and H1, respectively). The amplifier gains were automatically calibrated before the start of the whole session. Total analysis time for one spot was about 4.5 min.

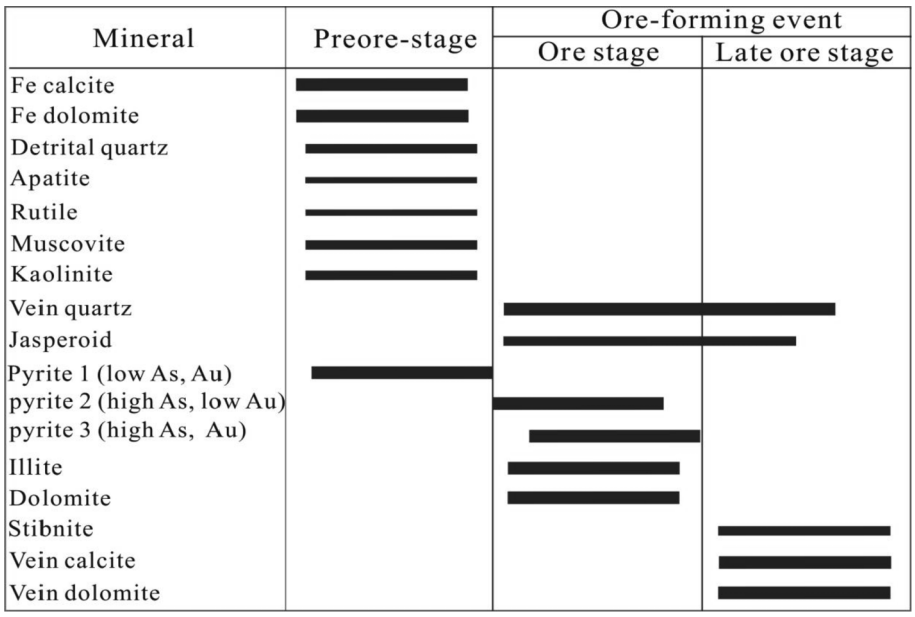

Fig. 6. Mineral paragenesis of the Linwang deposit.

5. Results

5.1. Pyrite type

Pyrite is the most abundant iron sulfide minerals in the Linwang deposit and is the main host mineral for gold (Chen et al., 2010; Gao et al., 2021). Based on pyrite morphology, texture, and chemistry, three types of pyrites are identified, including pre-ore pyrite (Py 1) and ore pyrites (Py 2 and Py 3) (Figs. 5 and 7).

Pre-ore pyrite (Py1) is framboidal (Fig. 7c), anhedral to euheral (Fig. 5c, f) pyrite and commonly occurs as a pyrite core with lower As and Au contents. This type of pyrite in the disseminated ores (Fig. 5g, j, and m) and pyrite veinlets (Fig. 7g) are partially replaced by As-rich and Au-poor pyrite 2 (Py 2; Figs. 5i, l, o, and 7h to l) .

Ore pyrites include an As-rich inner rim of pyrite (Py 2) and an Au-rich outer rim of pyrite (Py 3), which commonly formed overgrowth on the Py 1 (Figs. 5c, f, and 7h to l). The ore pyrites also formed individual, anhedral to euhedral pyrite crystals without the pyrite core (Py 1; Fig. 7h, k). The Py 2 and Py 3 are indistinguishable under the microscope as they have a similar yellowish-white color, bright reflectivity, and high relief. However, they are chemically distinct and can be distinguishable under backscattered electron (BSE) imaging adjusted for low brightness and high contrast; the Py 2 has brighter BSE imaging than that of the Py 3 and commonly rims the Py 1 (Fig. 5c, f) or replaced the Py 1 (Fig. 7h to l). The Py2 grains are anhedral to subhedral, with 5 to 30 μm in diameters. The Py 3 commonly rims the Py 2 and has subhedral to euhetral crystal faces, generally more than 20 μm in diameter. LA-ICP-MS analyses show that the Py 3 is the main host mineral for gold (Fig. 8e, f).

5.2. Pyrite geochemistry

A total of 289 spot analyses for trace elements were measured by LA-ICP-MS on the different types of pyrites from the Linwang deposit. The concentrations of trace elements in pyrites are included in Appendix 1 and displayed in Figs. 8–12. The average and median values of trace elements in each type of pyrite are listed in Table 2.

Pre-ore pyrite (Py 1) contains high Co (average = 299 ppm), Ni (1,229 ppm), Pb (369 ppm), Zn (5.89 ppm), and Bi (7.54 ppm) (Table 2), compared to the ore pyrites (Py 2 and Py 3), which contain low Co (average = 262 ppm to 68.9 ppm), Ni (978 ppm to 268 ppm), Pb (250 ppm to 149 ppm), Zn (1.29 ppm to 1.42 ppm), and Bi (5.38 ppm to 3.94 ppm). LA-ICP-MS spot analyses did detect Au in the Py 1 (Fig. 8a, b), with average of 11.6 ppm Au, As (36,739 ppm), Sb (245 ppm), Tl (0.94 ppm), Cu (493 ppm), and Se (35.7 ppm).

For ore pyrites (Table 2), the Py 2 (inner rim) has evaluated concentrations of Au (47.3 ppm), As (47,585 ppm), Sb (231 ppm), Tl (1.79 ppm), and Cu (799 ppm), and Se (41.0 ppm), compared to the Py 1. The trace element contents in the Py 3 (outer rim) contrasts with the Py 1 and Py 2 and has highest concentrations of Au (242 ppm), As (45,921 ppm), Sb (288 ppm), Tl (4.21 ppm), Cu (1,292 ppm), and Se (70.7 ppm).

All pyrites have similar range of Co/Ni ratios between 0.01 and 1 (Fig. 10f). Box- and -whisker diagram (Fig. 9) shows that the average and median concentrations of Au, As, Sb, Tl, Cu, and Se in the pyrites generally increase and Co, Ni, and Pb contents decrease from Py 1 to Py 3, with positive correlations between Au and As, Sb, Tl, Cu, and Se (Fig. 10). LA-ICP-MS mappings (Figs. 11 and 12) show that the pre-ore pyrite (Py 1) is generally enriched in Co-Ni-Pb-Bi-Sb ± As, whereas the ore pyrite is enriched in Au-As-Sb-Cu-Tl-Hg, with higher As and lower Au concentrations in the inner rims of ore pyrite (Py 2) and significantly higher As, Au contents in the outer rims of ore pyrite (Py 3).

5.3. Pyrite sulfur isotope compositions

A total of 121 data of sulfur isotope compositions measured by SIMS on the different types of pyrites from the Linwang deposit are included in Appendix 2 and showed on Figs. 7 and 13. The average and median values of $\delta^{33}S$, $\delta^{34}S$, and calculated $\Delta^{33}S$ in each type of pyrite are listed in Table 3.

The results show that all pyrites have similar ranges of $\delta^{33}S$, $\delta^{34}S$, and $\Delta^{33}S$ values (Fig. 13a). The pre-ore pyrite (Py 1) has $\delta^{34}S$ values ranging from +2.73‰ to +7.65‰ (average = +5.13‰) and $\delta^{33}S$ values of +1.49‰ to +3.89‰ (average = +2.64‰), with the $\Delta^{33}S$ values from −0.12 ‰ to +0.13‰ (Appendix 2 and Table 3). The $\delta^{34}S$ and $\delta^{33}S$ values of ore pyrite 2 (inner rim) range from +3.51‰ to +5.85‰ (average = +4.84‰), +1.89‰ to +3.11‰ (average = +2.52‰), respectively, with the $\Delta^{33}S$ values from −0.06‰ to +0.15‰. Ore pyrite 3 (outer rim) has similar ranges of $\delta^{34}S$ values (+3.80‰ to +6.09‰, average = +4.53‰) and $\delta^{33}S$ values (+2.00‰ to +3.10‰, average = +2.32‰), with the $\Delta^{33}S$ values from −0.18‰ to +0.14‰ as compared with the Py 1 and Py 2.

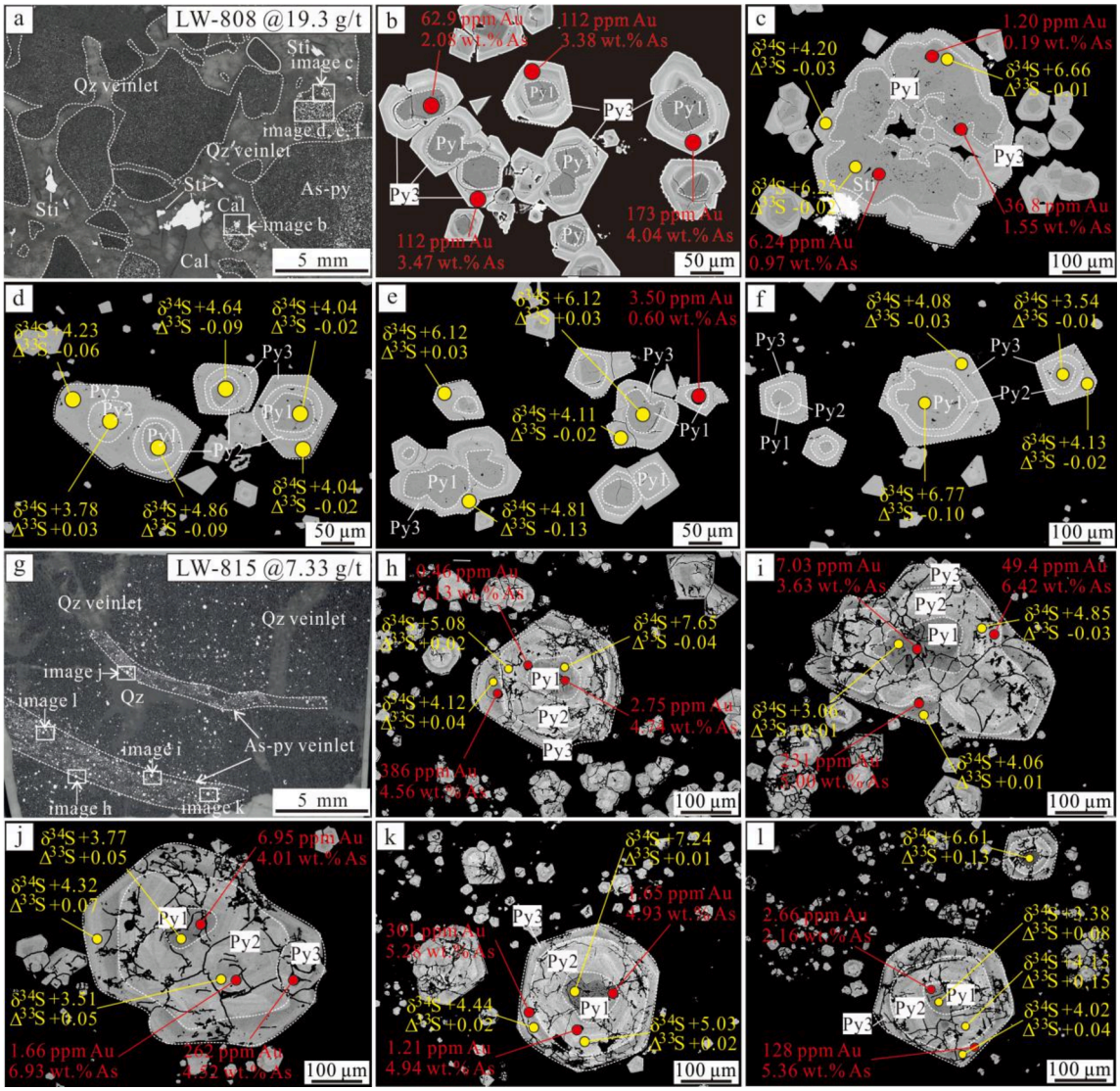

Fig. 7. Images of the locations for LA-ICP-MS trace element and SIMS S isotope analyses of the different pyrites from the Linwang deposit. Red dots indicate locations of LA-ICP-MS spot analyses, with Au and As concentrations. Yellow dots show the locations of SIMS S isotopes analyses, with $\delta^{34}S$ and $\Delta^{33}S$ values. (For interpretation of the references to color in this figure legend, the reader is referred to the web version of this article.)

6. Discussion

6.1. Pyrite formation

Pyrite is the most abundant iron sulfide minerals in Carlin-type gold deposits in the Youjiang basin and is the main host mineral for gold (Su et al., 2018). There are several generations of pyrite in the deposits, which have been described in detail by previous workers (Su et al., 2008, 2009a, b, 2012, 2018; Hou et al., 2016; Xie et al., 2018a, b; Li et al., 2020; Lin et al., 2021). Xie et al (2018b) outlines criteria for interpretation of pyrite timing based on occurrence, morphology, texture, and chemistry of pyrite: (1) pre-ore pyrite is framboidal and anhedral to euheral pyrite, dominated in low-/no-grade host rocks, and commonly occurs as a pyrite core with high Co, Ni and low As contents, which is interpreted a diagenetic origin; (2) ore-pyrite commonly rims pre-ore pyrite and contains an As-rich, Au-poor inner rim, and an As- and Au-rich outer rim, which are interpreted later hydrothermal origin.

For the Linwang deposit, pyrite formation can be divided into two stages: (1) pre-ore stage of pyrite and (2) hydrothermal stage of ore pyrite (Fig. 6). The pre-ore stage of pyrite consists of pyrite 1 (Py 1) and occurs as a core. It is commonly rimmed by ore pyrites (Py 2 and Py 3), demonstrating that it formed before the ore pyrites (Figs. 5c, f and 7c to f). The pre-ore pyrite has framboidal (Fig. 7c), anhedral to euheral textures (Fig. 5c, f), and contains higher average concentrations of Co, Ni, Pb, Zn, Bi, and lower As than those of the ore pyrites (Table 2), similar to the pre-ore pyrite in other Carlin-type gold deposits in the Youjiang basin, such as Shuiyindong, Jinfeng (Lannigou), Yata, and Jinya deposits (Hou et al., 2016; Xie et al., 2018a, b; Li et al., 2020; Lin et al., 2021). Large et al. (2009) and Gregory et al. (2015) used LA-ICP-MS to analysis global sedimentary (diagenetic and syngenetic) pyrites in carbonaceous shale and several sediment-hosted orogenic and Carlin-type gold deposits in Nevada and demonstrated that they contain abundant As, Ni, Pb, Cu, and Co. In addition, the Co/Ni ratio has been widely used to classify the origin of pyrite. Sedimentary pyrite generally exhibits low Co/Ni ratio of < 1 (Large et al., 2009; Gregory et al., 2015). Pre-ore pyrite in the Linwang deposit exhibits textural and chemical similarities and low Co/Ni ratio of < 1 to these sedimentary pyrites, suggesting that it formed during sedimentation and/or diagenesis.

Gold in the pre-ore pyrite (Py 1) was commonly detected in this study by LA-ICP-MS spot analyses (Fig. 8a, b). Gold concentrations in the Py 1 range from 1.82 ppm to 65.2 ppm ($n = 63$; Appendix 1 and Table 2), with average of 11.6 ppm Au, As (36,739 ppm), Sb (289 ppm), Tl

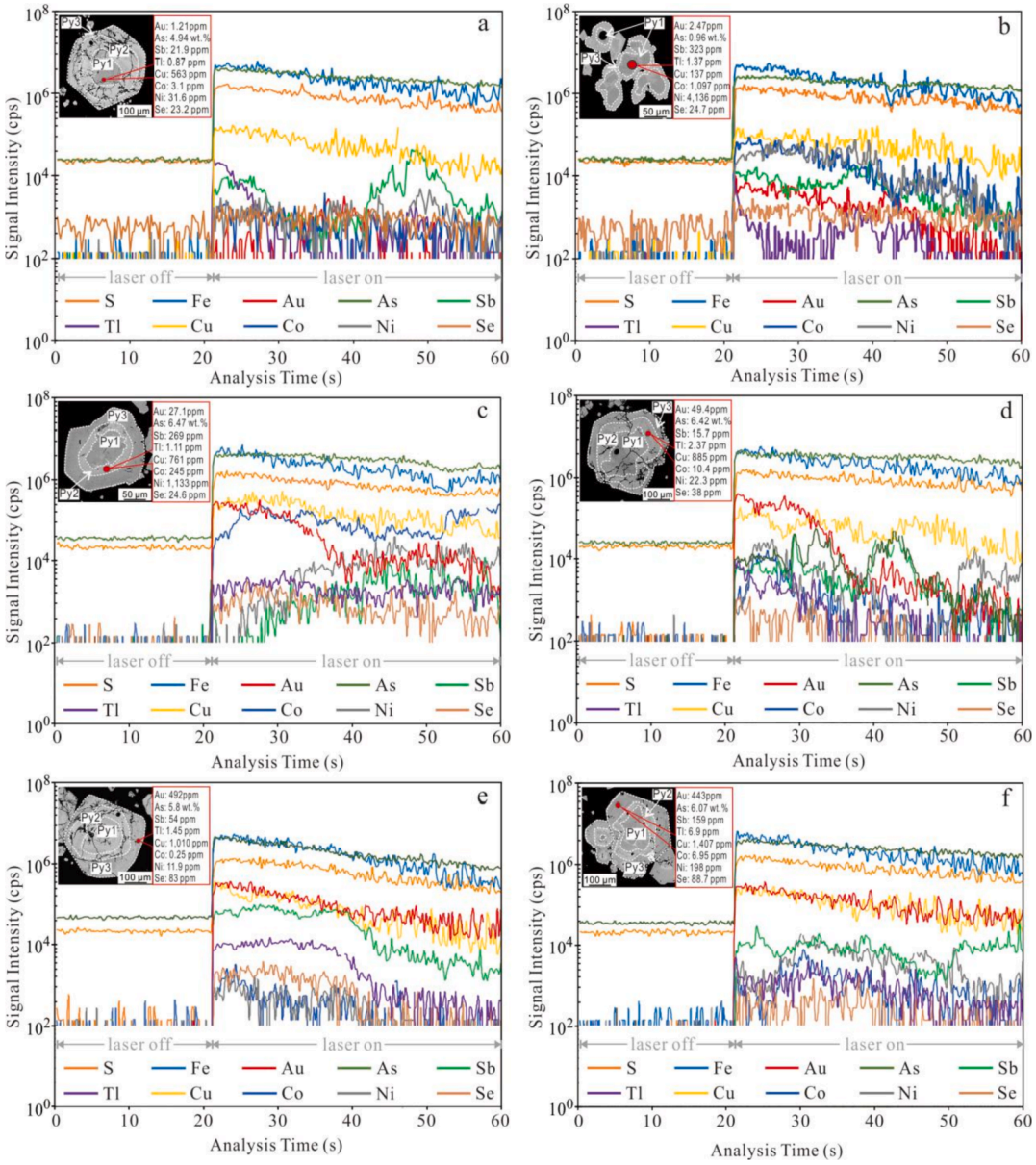

Fig. 8. Representative LA-ICP-MS time-resolved depth profiles for the Py 1 (a and b), Py 2 (c and d), and Py 3 (e and f) from the Linwang deposit.

(0.94 ppm), Cu (493 ppm), and Se (35.7 ppm). For comparison, we compiled available published LA-ICP-MS data of Au, As, and Sb contents for the pre-ore pyrites from other Carlin-type gold deposits in the Youjiang basin (Table 4 and Fig. 15), we found that the pre-ore pyrite in these deposits also contain ppm level of Au, with higher contents of As and Sb. For example, the pre-ore pyrites from the giant Shuiyindong deposit contain average of 2.12 ppm Au (n = 28), As (11,065 ppm), and Sb (111 ppm) (Hou et al., 2016; Jin, 2017; Xie et al., 2018b). In the north Carlin trend, Large et al. (2009, 2011) reported that the diagenetic pyrite in the carbonaceous sedimentary rocks contains higher Au (9.54 ppm to 168.71 ppm), As (2085.4 ppm to 6575.1 ppm), and Sb (531.5 ppm to 1239.9 ppm) and proposed that the diagenetic pyrite is a potential source of metals for formation of Carlin-type gold deposits in Nevada. The diagenetic pyrite in the Youjiang basin containing Au, As, and Sb supports this hypothesis, but more in situ data of Au, As, and Sb contents in the diagenetic pyrite from more deposits and districts in the Youjiang basin are needed to investigate in the future. Initial source of Au, As, and Sb enriched in the diagenetic pyrites in the Youjiang basin is unknown, they could be initially sourced from Permian Emeishan basalt or tuff, because the outcrops of magmatic rocks in the Youjiang basin are dominated by Permian Emeishan basalts, with thickness ranging from tens to hundreds of meters (Zhu et al., 2019). Petroleum exploration drillings also show that a thick sequence of the Emeishan basalts or tuff is buried hundreds of meters beneath the basin (Huang, 1986).

The pyrite textures, chemical zonation, and relationships to quartz ± stibnite veinlets (Fig. 5 a, g, m, and 7a, g) indicate that the ore pyrites in the Linwang were produced by later hydrothermal fluids. Hydrothermal ore pyrites commonly have an As-rich, Au-poor inner rim (Py 2) and an As- and Au-rich outer rim (Py 3). These textures have been observed in other Carlin-type gold deposits in the Youjiang basin, such as Jinfeng, Yata, and Jinya deposits (Hou et al., 2016; Xie et al., 2018a, b; Li et al., 2020; Lin et al., 2021). Xie et al. (2018a, b) interpreted the inner rim of pyrite in the Jinfeng deposit as the pre-ore pyrite and could have precipitated from an Au-free but As-rich of an early hydrothermal fluids or from low-Au and As-rich fluids at the beginning of the ore stage. However, in the Linwang deposit the inner rim of pyrite (Py 2) commonly contains Au (Table 2), with average of 47.3 ppm Au (n = 36), As (47,585 ppm), Sb (231 ppm), Tl (1.79 ppm), and Cu (799 ppm), and

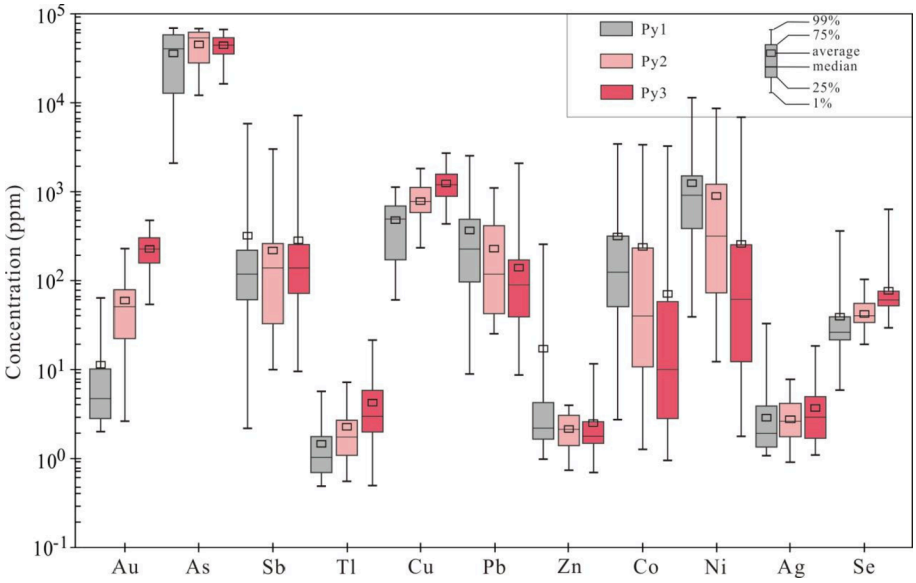

Fig. 9. Box- and -whisker diagram showing LA-ICP-MS trace element concentrations (Appendix 1) of the different pyrites from the Linwang deposit.

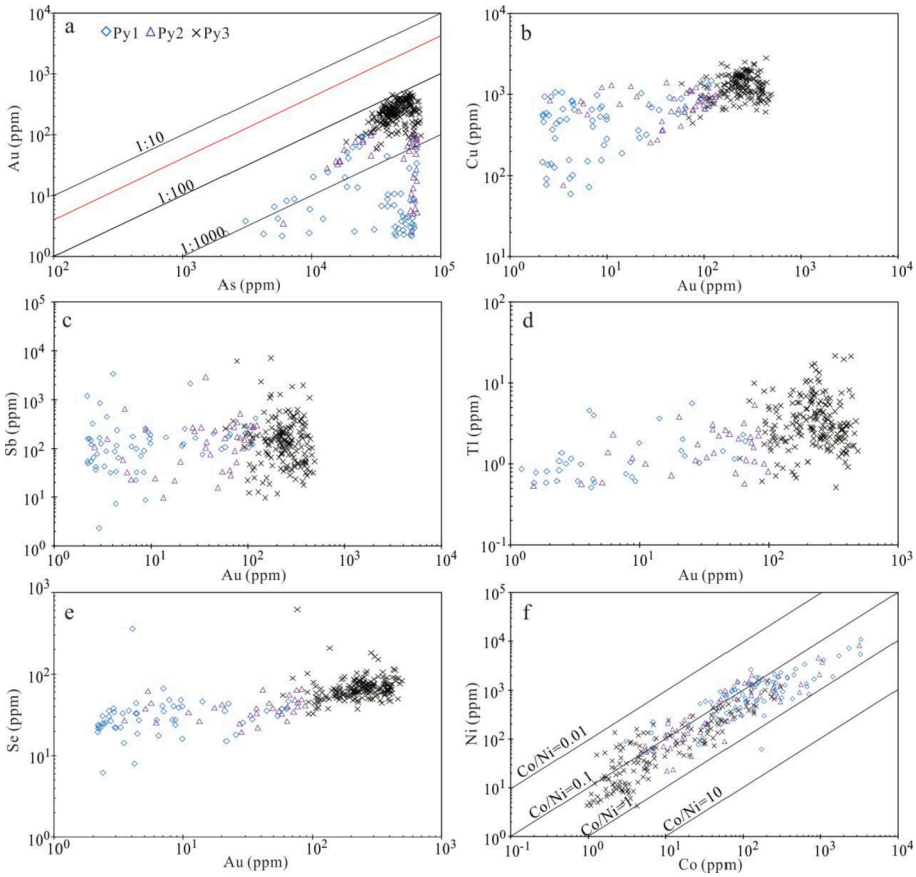

Fig. 10. Binary plots of selected trace elements in pyrite from the Linwang deposit. The red line in (a) represents is the solubility limit of gold in pyrite (Reich et al., 2005). (For interpretation of the references to color in this figure legend, the reader is referred to the web version of this article.)

Se (41.0 ppm). We interpret that the inner rim of pyrite in the Linwang deposit precipitated from the ore fluids at the beginning of the ore stage, following deposition of the outer rim of pyrite (Py 3) on the Py 2, with higher Au (242 ppm, n = 191), As (45,921 ppm), Sb (288 ppm), Tl (4.21 ppm), Cu (1292 ppm), and Se (70.7 ppm). This suggestion is evidenced by continuous growth of small pyrite crystals (Fig. 7h) and a lack of replacement at the interface between the Py 2 and Py 3 (Figs. 5 c, f, l, and 7f, k). On the Au vs. As diagram (Fig. 10 a), all pyrites form a wedge-shaped zone and plot below the solubility limit of gold in pyrite determined by Reich et al. (2005), suggesting that Au may occur as invisible form of structurally bounded Au^{1+} in pyrites.

The mechanism attributing to chemical differences of Py 2 (inner

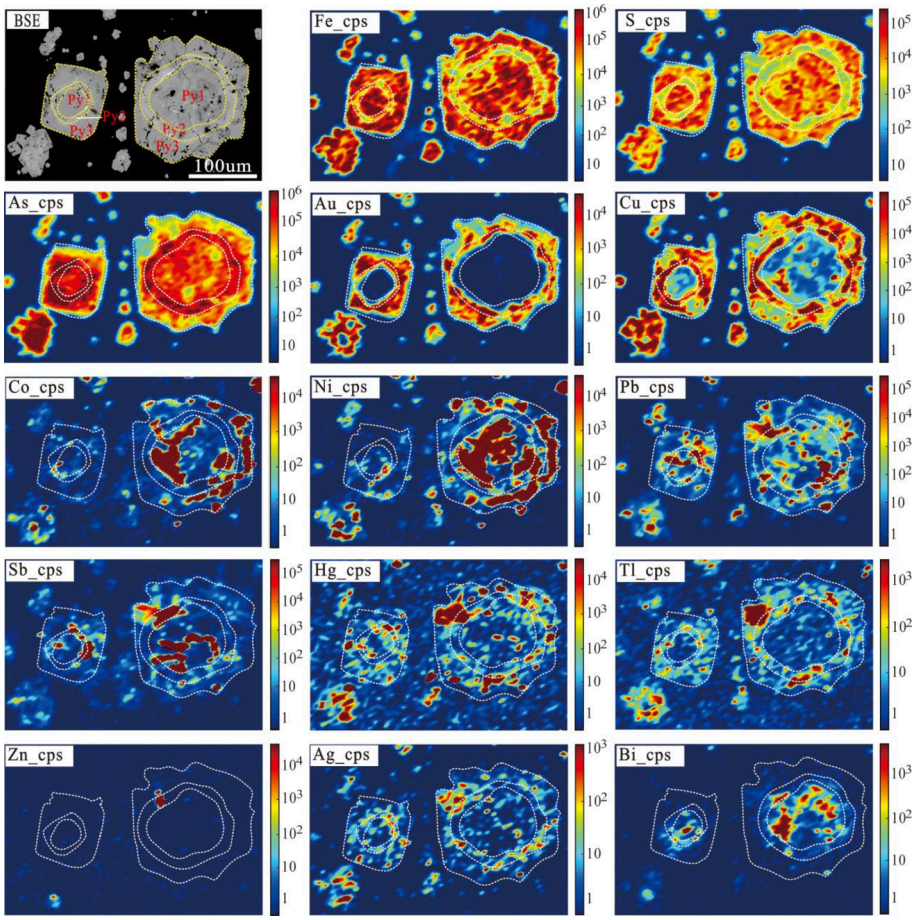

Fig. 11. SEM image and LA-ICP-MS maps showing the distributions of trace elements in a pyrite from the Linwang deposit.

rim) and Py 3 (outer rim) in the Linwang deposit as well as other Carlin-type gold deposits in the Youjiang basin is unknown. Liang et al. (2021) used the focused ion beam combined with scanning electron microscope (FIB-SEM) and transmission electron microscope (TEM) techniques to examine invisible gold in arsenian pyrite from the Shuiyindong and Jinfeng deposits in the Youjiang basin and Getchell and Cortez hills deposits in Nevada. This study confirmed that the ore pyrite in the Carlin-type gold system was formed during rapid crystallization and Au was principally incorporated into the crystal structure of arsenian pyrite (Reich et al., 2005; Kusebauch et al., 2018, 2019; Muntean and Cline, 2018). The process of rapid pyrite crystallization requires significant changes in ore fluid conditions (e.g. temperature, pressure, and/or mixing with other fluids). Fluid inclusion measurement and oxygen and hydrogen isotope compositions of ore fluids for the Linwang deposit (Luo et al., 2019), as well as other Carlin-type gold deposits in the Youjiang basin (Su et al., 2009a, 2018), indicate no significant changes in temperature (230 ± 30 °C) for the ore fluids and mixing with other fluids, suggesting that the temperature change of the ore fluids and mixing with other fluids are not the main factor attributing to chemical differences of the ore pyrites (Py 2 and Py 3). High-grade ores (Fig. 4c, d) in the Linwang deposit are spatially associated with hydraulic brecciation of silicified wall rocks, implying higher pressure of the ore fluids that can permeate and reacted with the ferroan dolomite cements and partially replaced the pre-ore (diagenetic) pyrite in the host rocks, possibly forming the inner rim of pyrite (Py 2) at the beginning of the ore stage. Rapid drops in pressure resulting from fault failure may lead to the more ore fluids flowed upward into structural highs where they reacted with Fe-bearing minerals in the host rocks to precipitate the outer rim of Au-rich pyrite (Py 3) on the Py 2.

6.2. Sources of sulfur and metals

In the Carlin-type gold system, ore fluids were enriched in reduced S (Hofstra et al., 1991; Hofstra and Cline, 2000; Su et al., 2009a, 2018; Muntean and Cline, 2018). As gold was principally transported as a bisulfide complex (Seward, 1973, 1991; Stefánsson and Seward, 2004), Au cannot have been sourced at depths than the S, the S isotope data can provide insights into Au sources (Hou et al., 2016).

Sulfur isotopic signature ($\delta^{34}S$) of sulfide has been used for decades to constrain sulfur sources and processes in hydrothermal ore deposits (Ohmoto, 1972). However, the $\delta^{34}S$ signature is sensitive to a range of mineralizing processes, it is difficult to interpret the $\delta^{34}S$ data and distinguish between the influence of the sulfur source reservoirs and the effect of changes in thermodynamic conditions affecting the sulfur-bearing fluid as it is transported and deposited (Sugiono et al., 2021), making it not be an unambiguous constraint on the sulfur source for hydrothermal ore deposits (Santiago et al., 2021).

In most chemical reactions, the sulfur isotope ratios obey mass-dependent fractionations (MDF); however, significant mass-independent fractionation (MIF, $\Delta^{33}S$) anomalies were identified in pyrite and barite from Archean sedimentary rocks, which was caused by SO_2 photolysis in the atmosphere (Farquhar et al., 2000; Pavlov and Kasting, 2002: Bekker et al., 2004; Ohmoto et al., 2007; Johnston, 2011; Masterson et al., 2011; Philippot et al., 2012). The MIF-S signature is also known to persist through magmatic recycling processes. It has been detected within lavas associated with mantle plumes (Cabral et al., 2013) and magmatic intrusions (LaFlamme et al., 2018) and in diamond-hosted inclusions (Smit et al., 2019), which is interpreted to be recycled from subducting slabs of Archean crust. The MIF-S signature adds another dimension to direct constraint on sulfur source for

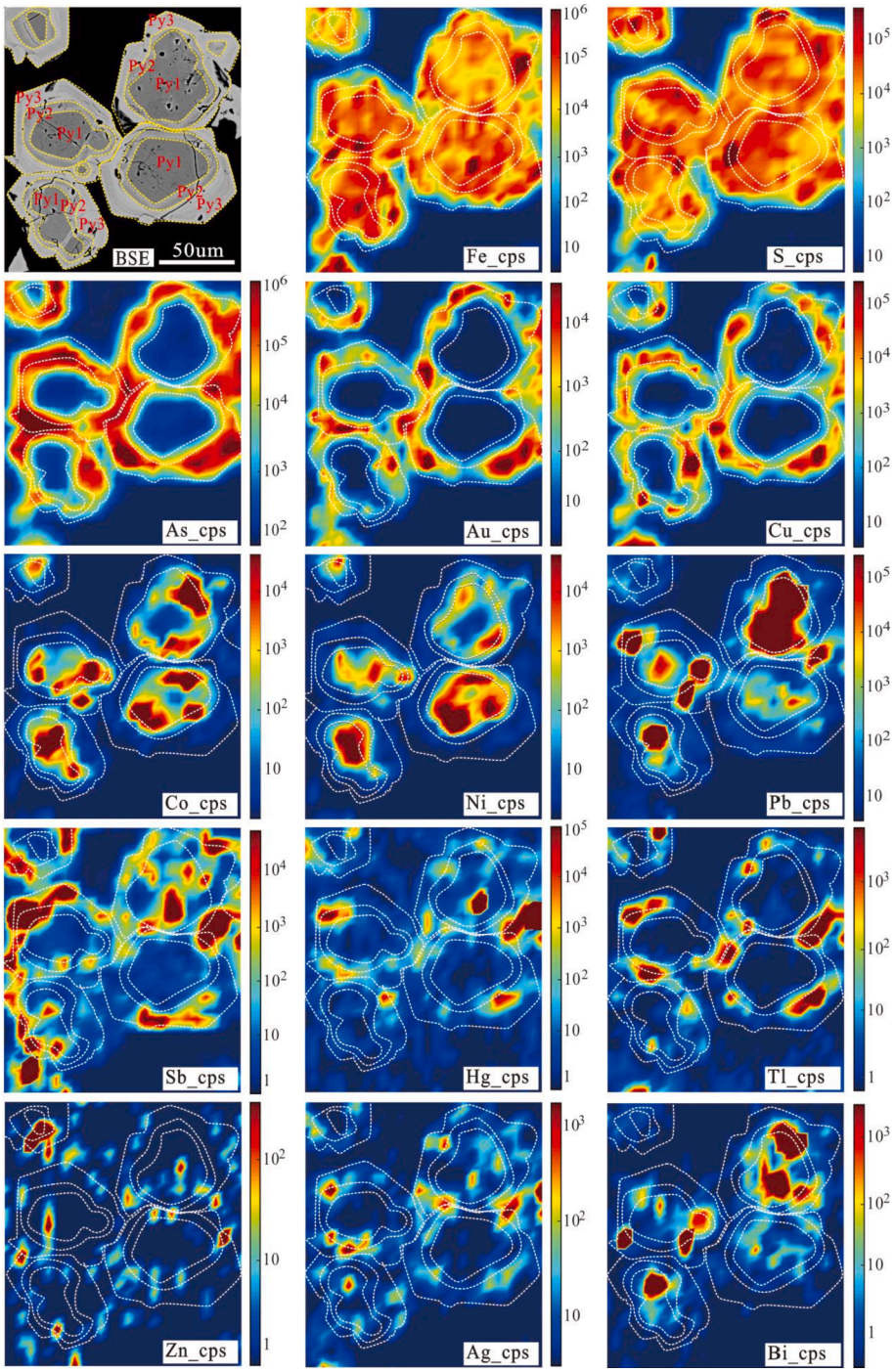

Fig. 12. SEM image and LA-ICP-MS maps showing the distributions of trace elements in another pyrite from the Linwang deposit.

orogenic gold system (Xue et al., 2013; Steadman et al., 2015; Agangi et al., 2016; Gregory et al., 2016; Selvaraja et al., 2017a, b, c; LaFlamme et al., 2018; Sugiono et al., 2021).

In the Linwang deposit, all pyrites have narrow range of $\delta^{34}S$ values (Fig. 13a; Table 3), with average of +5.13‰ for pre-ore pyrite 1, +4.84‰ for ore pyrite 2 (inner rim), and +4.53‰ for ore pyrite 3 (outer rim), suggesting the S of ore pyrites was mainly derived from a sedimentary source. In addition, all data of $\delta^{33}S$ and $\delta^{34}S$ for pyrites are plotted on the mass-dependent fractionation (MDF) line (Fig. 13b; $\delta^{33}S = 0.515 \times \delta^{34}S$, Hulston and Thode, 1965). A near zero $\Delta^{33}S$ signature in all pyrites in the Linwang deposit (Table 3) indicates no record of the assimilation of Archean sulfur that have MIF-S signatures in the Archean sedimentary or metamorphic rocks, implying the deep basement of Archean rocks beneath the basin were not involved the formation of the Linwang deposit. On the $\Delta^{33}S$ vs. $\delta^{34}S$ diagrams (Fig. 13c, d), all pyrites are plotted between a volcanic SO_2 (Ono et al., 2003) and Permian seawater sulfate reservoirs (Zhang et al., 2015), and overlap with sedimentary pyrites in Permian-Triassic boundary in South China (Zhang et al., 2015; Saitoh et al., 2017), but have different array of $\Delta^{33}S$-$\delta^{34}S$ from the ore-related pyrites and sedimentary pyrites in Permian Maokou and Heshan or Wujiaping Formations in the Youjiang basin (Zhang et al., 2015). These data suggest that the S within the Linwang deposit was most likely sourced from the Triassic sedimentary rocks that host the deposit rather than the Permian sedimentary rocks. In addition, the diagenetic pyrites (Py 1) in the Linwang commonly contain ppm level of Au, with higher contents of As and Sb (Fig. 15), suggesting

Table 2
Summary of LA-ICP-MS data of average and median values (ppm) of trace elements in each type of pyrite from the Linwang deposit.

Type	Stage	Analyses no.	Au ~0.03*	As ~20*	Sb ~0.04*	Tl ~0.01*	Cu ~0.80*	Pb ~0.12*	Zn ~0.45*	Co ~0.51*	Ni ~0.59*	Se ~0.69*	Ag ~0.01*	Bi ~0.01*
	Average value													
Py1	Pre-ore	N = 63	11.6	36,739	245	0.94	493	369	5.89	299	1229	35.7	2.35	7.54
Py2	Ore	N = 36	47.3	47,585	231	1.79	799	250	1.29	262	978	41.0	2.36	5.38
Py3	Ore	N = 191	242	45,921	288	4.21	1292	149	1.42	68.9	268	70.7	3.90	3.94
	Median value													
Py1	Pre-ore	N = 63	4.37	44,107	119	0.59	496	216	1.18	147	866	27.6	1.38	4.92
Py2	Ore	N = 36	46.2	59,074	107	1.40	761	112	1.09	49.1	290	39.7	2.04	3.52
Py3	Ore	N = 191	231	44,462	146	2.99	1231	97.1	1.12	6.47	66.1	63.4	3.41	1.42

Notes: Data used to calculate the average and median values are listed in Appendix 1
*Value listed below the element is the detection limit (in ppm).

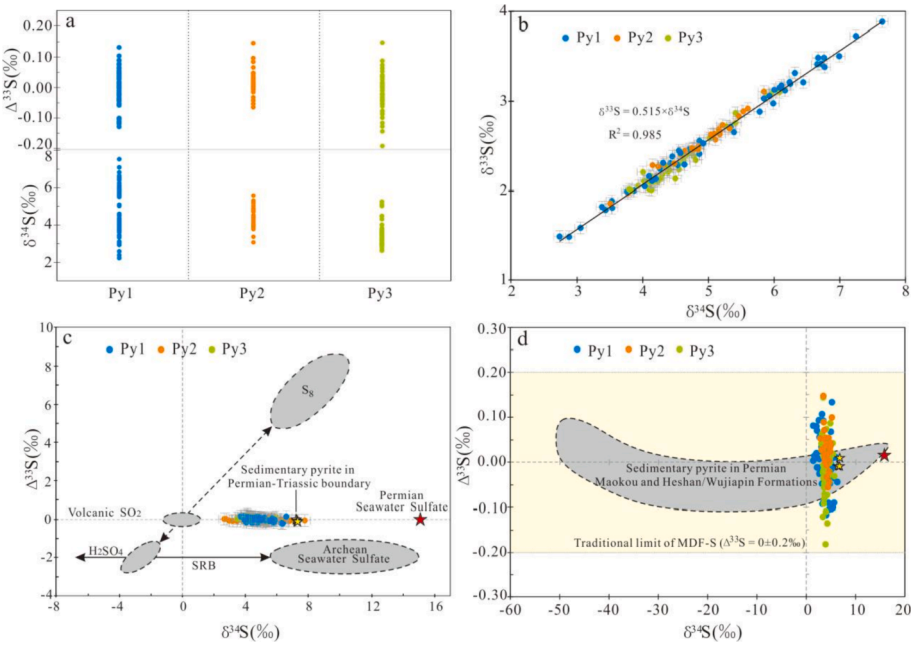

Fig. 13. Multiple sulfur isotope systematics for the different generations of pyrites in the Linwang deposit. (a) Spread of $\Delta^{33}S$ and $\delta^{34}S$ values on the different generations of pyrites. (b) Plot of $\delta^{34}S$ vs. $\delta^{33}S$ for the different generations of pyrites, note that the all data were plotted on the mass-dependent fractionation (MDF-S) line ($\delta^{33}S = 0.515 \times \delta^{34}S$, Hulston and Thode, 1965). (c) Plot of $\delta^{34}S$ vs. $\Delta^{33}S$ for the different generations of pyrites. Gray fields represent S isotopic compositions of volcanic SO_2, S_8 and H_2SO_4, and seawater sulfate in the Archean sedimentary rocks (Ono et al., 2003). SRB represents sulfate reducing bacteria. Red star indicates Permian seawater sulfate (Zhang et al., 2015). Yellow star represents sedimentary pyrite in Permian-Triassic boundary in South China (Zhang et al., 2015; Saitoh et al., 2017). (d) Comparison of $\delta^{34}S$ and $\Delta^{33}S$ values for the ore-related pyrites and Permian sedimentary pyrites in the Maokou and Heshan Formations in the Youjiang basin. Note that they have different array of $\delta^{34}S$ - $\Delta^{33}S$. Yellow field represents traditional limit of mass dependent fractionation of sulfur (MDF-S) ($\Delta^{33}S = 0 \pm 0.2‰$) from Farquhar and Wing (2003). (For interpretation of the references to color in this figure legend, the reader is referred to the web version of this article.)

Table 3
Summary of SIMS data of average and median values (‰) of S isotopes in each type of pyrite from the Linwang deposit.

Type	Stage	Analyses no.	$\delta^{33}S$ (‰)	2SE	$\delta^{34}S$ (‰)	2SE	$\Delta^{33}S$ (‰)	2SE
	Average							
Py1	Pre-ore	N = 48	2.64	0.08	5.13	0.13	0.003	0.06
Py2	Ore	N = 28	2.52	0.08	4.84	0.13	0.03	0.06
Py3	Ore	N = 45	2.32	0.08	4.53	0.13	−0.02	0.06
	Median							
Py1	Pre-ore	N = 48	2.53	0.08	4.87	0.13	0.01	0.06
Py2	Ore	N = 28	2.53	0.08	4.95	0.13	0.03	0.06
Py3	Ore	N = 45	2.23	0.08	4.39	0.13	−0.02	0.06

Abbreviations: Py1 = Pre-ore pyrite 1, Py2 = Ore pyrite 2 (inner rim), Py3 = Ore pyrite 3 (outer rim).
$\Delta^{33}S = \delta^{33}S - (1000 \times ((1 + \delta^{34}S/1000)^{0.515} - 1))$

that the diagenetic pyrites in the host rocks are a potential source of Au for the formation of the Linwang deposit.

In the other Carlin-type gold deposits in the Youjiang basin, available in-situ $\delta^{34}S$ data for the pre-ore and ore pyrites are compiled from the literatures for comparison (Fig. 14). The $\delta^{34}S$ values of the pre-ore and ore pyrites varied significantly within and between mining districts. For example, the deposits on the platform that host in the Permian bioclastic limestone, siltstone and argillite (e. g. Shuiyindong and Taipingdong) and the Permian basalt tuff or volcaniclastic rocks (e. g. Nibao) have a broad range of $\delta^{34}S$ values (−33.8‰ to +17.9‰) for the pre-ore pyrites, and a narrow range of $\delta^{34}S$ values (−5‰ to +5‰) for the ore pyrites (Hou et al., 2016; Hu et al., 2018; Xie et al., 2018a, b; Li et al., 2020; Liang et al., 2020; Zhao et al., 2020; Wei et al., 2020; Lin et al., 2021). Such a broad variation of $\delta^{34}S$ values for the pre-ore pyrites is consistent with sedimentary pyrites (−48.5‰ to +15.1‰) in the Permian Maokou and Heshan or Wujiaping Formations in South China (Zhang et al., 2015). In the central basin, the deposits that host in the Triassic siliciclastic rocks have a narrow range of $\delta^{34}S$ values for the pre-ore and ore

Table 4
LA-ICP-MS data of average and median values (ppm) of Au, As and Sb contents in the pre-ore pyrites from Carlin-type gold deposits in the Youjiang basin.

Deposit	Au (ppm)	As (ppm)	Sb (ppm)	References
Nibao	0.013 to	31 to 3,464	0.007 to	Jin, 2017; Lin et al.,
	2.9	Average	72.7	2021
	Average	1,288.3	Average	
	1.7	Median 884	18.4	
	Median	n = 7	Median	
	0.6		4.6	
	n = 5		n = 9	
Shuiyindong	0.06 to	53 to	4.7 to	Hou et al., 2016; Jin,
	11.65	71,035.9	460.1	2017; Xie et al., 2018b
	Average	Average	Average	
	2.12	11,064.8	110.7	
	Median	Median	Median	
	0.81	5,062.1	78.2	
	n = 28	n = 51	n = 41	
Taipingdong	0.09 to	5,128.9 to	26.5 to	Hou et al., 2016
	1.72	23,399.8	558.2	
	Average	Average	Average	
	0.72	13,466	190.8	
	Median	Median	Median	
	0.53	12,911.1	101.5	
	n = 8	n = 8	n = 8	
Getang	0.06 to	78.4 to	0.38 to	Hu et al., 2018
	4.01	2,926	126	
	Average	Average	Average	
	1.07	715.6	29.7	
	Median	Median	Median	
	0.7	219.6	8.91	
	n = 33	n = 33	n = 33	
Lannigou	2.3 to 8.8	348.4 to	20.4 to	Xie et al., 2018b
	Average	19,774.3	532.6	
	4.73	Average	Average	
	Median	5,628.35	213.9	
	3.9	Median	Median	
	n = 4	2,017.5	167.2	
		n = 14	n = 14	
Yata	1.3 to 6.9	1,293 to	40.8 to	Jin , 2017
	Average	17,770	448.2	
	2.85	Average	Average	
	Median	8,738.2	166.1	
	2.3	Median	Median	
	n = 10	6,757	138.3	
		n = 17	n = 17	
Linwang	1.82 to	2,155 to	2.32 to	This study
	65.2	64,919.4	3,372	
	Average	Average	Average	
	11.6	36,739	289.2	
	Median	Median	Median	
	4.37	44,107	119.3	
	n = 63	n = 63	n = 63	
Jinya	0.02 to	2,580 to	21 to 367	Li et al., 2021
	0.48	18,500	Average	
	Average	Average	139.7	
	0.17	18,500	Median	
	Median	Median	124	
	0.08	8,188	n = 30	
	n = 29	n = 30		

pyrites in each deposit, such as Lannigou, Yata, Banqi, and Jinya deposits. Hou et al. (2016) and Xie et al. (2018b) interpreted the broad range of $\delta^{34}S$ values for the pre-ore pyrites as the result of bacterial reduction from marine sulfate during sedimentation and diagenesis, and the narrow range of $\delta^{34}S$ values for the ore pyrites is a deep magmatic S source for the ore fluids.

Although the $\delta^{34}S$ values for the pre-ore and ore pyrites in each deposit are variable, however, the median of $\delta^{34}S$ values for the ore pyrites overlap with that of the pre-ore pyrites (Fig. 14). In addition, the diagenetic pyrites in other deposits in the Youjiang basin also contain ppm level of Au, with higher contents of As and Sb (Fig. 15). These data also suggest that the S and Au were mainly derived from a sedimentary source rather than a deep magmatic S source, because no coeval felsic intrusive rocks were observed in the Youjiang basin or in the vicinity of the deposits.

6.3. Source of ore fluids and precipitation processes

As quartz veinlets are spatially associated with high-grade ores in the Linwang deposit (Fig. 4), it is inferred that these veinlets are ore related. Fluid inclusion measurement and oxygen and hydrogen isotope compositions of quartz veinlets from the Linwang have been reported by Luo et al. (2019). The quartz veinlets contain two-phase, liquid-rich aqueous and two- or three-phase aqueous-carbonic fluid inclusions, with an average homogenization temperature of 230 °C and salinity of 5.4 wt% NaCl equiv., similar to other deposits in the Youjiang basin (Su et al., 2009a, 2018). They have a narrow range of high $\delta^{18}O$ values (21.7‰ to 26.5‰). Calculated $\delta^{18}O_{H2O}$ values for fluids vary from +11.7‰ to +16.5‰ at 230 °C; the measured δD_{H2O} values of water extracted from fluid inclusions in the quartz veinlets range from −71‰ to −57‰, which plot within or close to the metamorphic-water box on the $\delta^{18}O_{H2O}$ – δD_{H2O} diagram (Luo et al., 2019, Fig. 5), suggesting that the ore fluids of the Linwang deposit are consisted predominantly of metamorphic fluids.

The Linwang deposit shares many characteristics with other Carlin-type gold deposits in the Youjiang basin, including the host rocks, mineral assemblages, alteration types, element associations, and residence of gold. It may have ore precipitation mechanisms similar to other deposits. Petrographic observations show that the ferroan dolomite cements in sandstone and siltstone formed during sedimentation are partially replaced by quartz and followed by deposition of tiny arsenian pyrite and illite in pore space (Fig. 5h, k), indicating that the ore precipitation processes of the Linwang are similar to other deposits in the Youjiang basin in that gold and pyrite precipitated together from H_2S-rich, Fe-poor fluids that reacted with Fe-bearing minerals in the host rocks (Su et al., 2009a, 2018; Xie et al., 2018a, b). Arsenic, Cu, Sb, and Tl were incorporated into the ore pyrites during sulfidation process. Locally, irregular boundaries between the pre-ore and ore pyrites (Fig. 7h to l) suggest that replacement in addition to sulfidation may have been important in the formation of ore pyrites.

Although accurate age of gold mineralization for the Linwang deposit is not constrained by isotope dating, a zircon U-Th/He age of 133 Ma from the mineralized rocks in the Linwang has been reported by Gao et al. (2021) and is interpreted as gold mineralization age, corresponding to Yanshanian orogeny. Oxygen and hydrogen isotopes of ore fluids indicate a metamorphic origin (Luo et al., 2019). Such metamorphic ore fluids were generated by regional metamorphism of sedimentary rocks, possibly related to crustal thickening and prograde metamorphism during the late Yanshanian orogeny (Su et al., 2009a, 2018). The ore fluids were focused into the main fault zones and then flowed upward into structural highs in response to stress relaxation during the orogeny. Gold and pyrite precipitated together where the ore fluids reacted with Fe-bearing minerals in the host rocks to have formed the Linwang deposit.

7. Conclusions

The results of this study of pyrite textures, paragenesis and multiple S isotopes and trace element geochemistry at the Linwang deposit support the model of Su et al. (2009a, 2018), who suggested that the S and Au were introduced by metamorphic fluids for the Carlin-type gold mineralization in the Youjiang basin.

Our results have clearly shown that Au was initially trapped in the structure of fine-grained (framboidal) sedimentary and diagenetic forms of arsenian pyrite (Py 1) within the siltstone and mudstone during sedimentation and diagenesis. Late compressional tectonic event associated with the Yanshanian orogeny could led to the release of Au, As and Sb from previously dissolved in the diagenetic pyrite (Py 1) to the metamorphic fluids. Such fluids were focused into the main fault zones and flowed upward into structural highs in response to stress relaxation during the orogeny. Gold and pyrite precipitated together where the ore

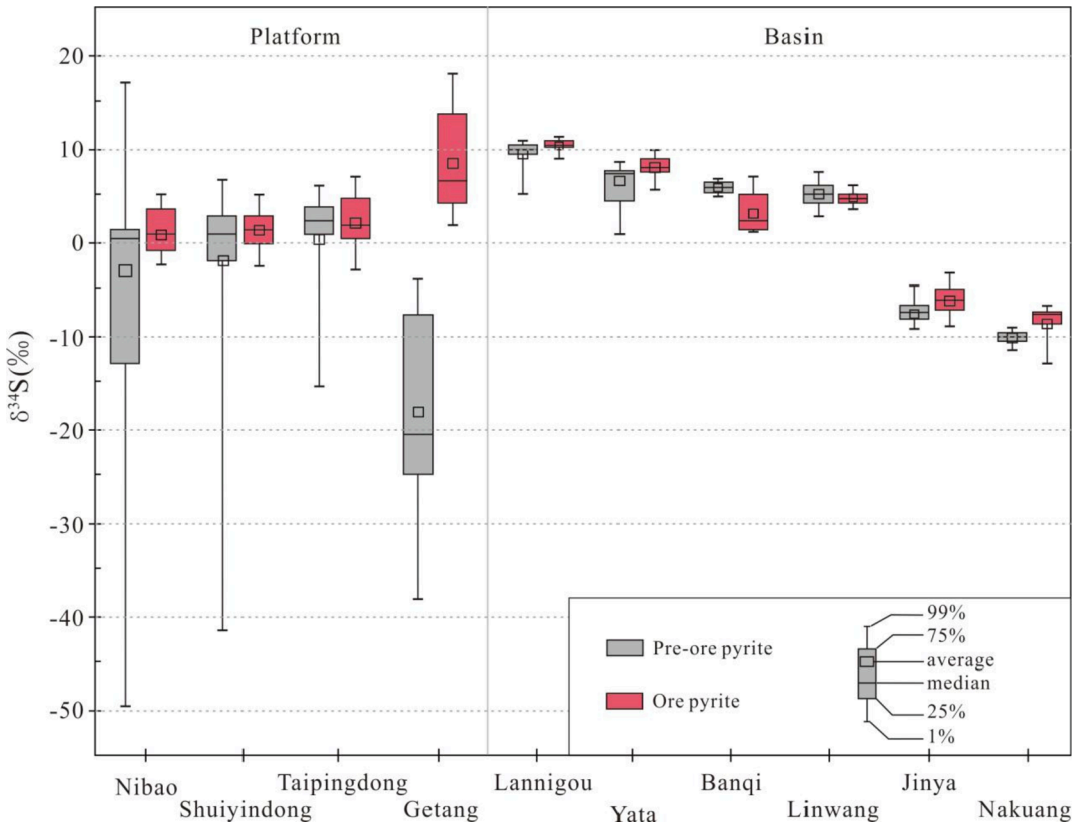

Fig. 14. Compilation of $\delta^{34}S$ data for the pre-ore and ore pyrites from the Carlin-type gold deposits in the Youjiang basin. Sulfur isotopic data for the pre-ore and ore pyrites were obtained from in situ SHRIMP, LA-MC-ICP-MS, and NanoSIMS analyses. Data are from Hou et al. (2016), Jin (2017), Wu (2018), Xie et al.(2018b), Hu et al. (2018), Li et al. (2020), Zhao et al. (2020), Li et al. (2021), Liu et al. (2021) and this study.

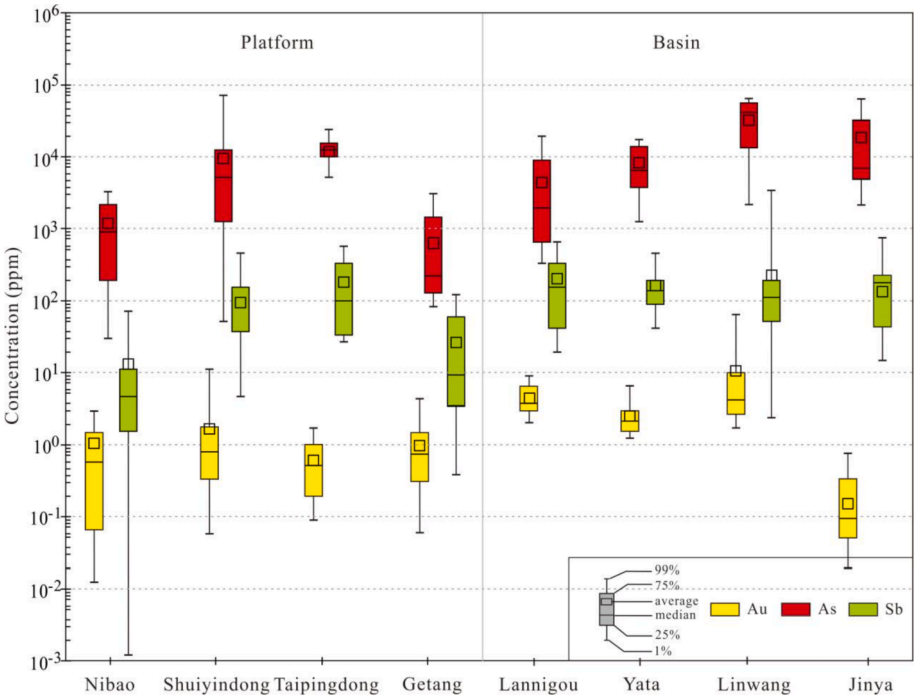

Fig. 15. Compilation of Au, As and Sb contents for pre-ore pyrites (diagenetic pyrite) from the Carlin-type gold deposits in the Youjiang basin. Trace elements data for the pre-ore pyrites were obtained from LA-ICP-MS analyses. Data are from Hou et al. (2016), Jin (2017), Xie et al.(2018a, Xie et al., 2018b), Hu et al. (2018), Li et al. (2021), Lin et al. (2021) and this study,

fluids reacted with Fe-bearing minerals in the host rocks, which commenced with the deposition of As-rich pyrite (Py 2), followed by Au-rich pyrite (Py 3).

This two-stage process of sedimentary (diagenetic) Au-bearing arsenian pyrite and gold deposition is key to the formation of the Linwang deposit and may apply to the genesis of other Carlin-type gold deposits in the Youjiang basin.

Declaration of Competing Interest

The authors declare that they have no known competing financial interests or personal relationships that could have appeared to influence the work reported in this paper.

Acknowledgments

We are grateful to Guangxi Dashiwei Gold Mines for access to samples and to Sixue Yue for geological guidance and discussions during fieldwork. We would like to thank Shaohua Dong and Xiang Li for their help with electron microprobe and scanning electron microprobe analyses, and Haiyang Li and Zexian Cui for their help with LA-ICP-MS and SIMS analyses. Dr. Xinghui Li and an anonymous reviewer are particularly thanked for reviews that clarified and improved presentation and scientific arguments. This work was supported by the National Natural Science Foundation of China (U1812402, 41772079).

Appendix

Appendix 1
LA-ICP-MS trace element concentrations (ppm) of pyrites from the Linwang gold deposit.

Analysis no.	Pyrite type	Stage	Au	As	Sb	Tl	Cu	Pb	Zn	Co	Ni	Se	Ag	Bi
			~0.03*	~20 *	~0.04 *	~0.01*	~0.80 *	~0.12*	~0.45*	~0.51*	~0.59*	~0.69*	~0.01*	~0.01*
LW-802@12.3 g/t														
LW-802–1	Py1	Pre-ore	9.88	44,009	127	0.25	498	116	1.19	86.7	959	40.2	1.19	6.06
LW-802–2			1.82	57,154	69.1	0.29	680	49	1.24	207	1363	18.1	0.84	4.83
LW-802–3			34.2	64,598	75.2	0.43	643	59	0.77	33.0	590	27.9	0.69	2.28
LW-802–4			58.1	64,919	106	0.45	886	102	1.13	145	598	37.6	1.30	4.01
LW-802–5			8.75	62,078	8.71	0.26	715	9	1.28	187	595	27.3	0.43	2.39
LW-802–6			22.4	62,870	252	1.26	1034	216	1.26	50.4	419	43.3	2.13	3.82
LW-802–7			2.92	44,410	165	1.16	289	202	1.33	26.8	75.9	34.1	1.74	8.59
LW-802–8			9.88	48,709	189	1.82	283	194	0.77	172	61.1	16.1	1.80	4.92
LW-802–9			8.39	57,932	32.3	0.22	674	23	1.18	45.2	420	27.6	0.45	2.17
LW-802–10			1.91	60,400	289	0.81	1034	107	22.3	251	1171	18.4	1.73	14.38
LW-802–11			2.51	50,774	65.1	0.41	555	74	0.79	478	2694	25.5	0.79	8.88
LW-802–12			3.01	58,049	125	0.37	438	95	1.40	4.39	38.2	21.9	1.12	1.72
LW-802–13			2.28	57,960	159	0.61	939	129	2.34	308	2308	22.2	1.25	7.49
LW-802–14			9.64	39,439	159	0.29	530	300	0.65	83.3	623	48.4	1.36	10.90
LW-802–15	Py2	Ore	5.33	65,805	648	0.35	833	484	0.88	21.8	44.5	61.9	1.79	2.45
LW-802–16			8.75	60,768	243	1.19	1227	187	1.23	34.1	201	52.6	2.50	4.37
LW-802–17			64.4	63,021	36.3	0.57	721	27	0.66	28.3	136	39.7	0.71	1.10
LW-802–18			91.6	64,820	149	1.01	817	111	0.87	4.40	12.9	52.8	1.75	1.92
LW-802–19			2.59	59,074	107	0.29	843	110	0.89	179	1711	31.7	1.18	10.77
LW-802–20			5.10	60,846	58.7	0.59	625	78	1.78	63.1	234	37.5	0.94	4.98
LW-802–21	Py3	Ore	222	68,174	215	2.07	1723	157	0.76	0.60	2.51	103	3.49	1.61
LW-802–22			394	54,059	336	2.37	1103	231	0.82	0.76	3.27	73.4	3.94	0.56
LW-802–23			330	58,140	50.3	1.84	1556	24	1.26	1.31	6.63	64.6	1.64	0.60
LW-802–24			367	45,956	163	7.58	900	78	1.31	2.11	8.40	56.7	5.04	0.77
LW-802–25			398	58,076	63.1	1.55	1261	53	0.91	1.51	15.1	63.4	1.92	0.30
LW-802–26			216	58,644	128	2.61	986	118	1.20	233	731	49.6	2.99	5.66
LW-802–27			274	61,940	112	3.36	1334	102	0.76	28.0	92.9	76.1	3.20	2.74
LW-802–28			372	53,864	239	2.64	1314	145	1.84	1.09	4.31	68.7	3.90	0.70
LW-802–29			385	50,224	78.0	2.42	807	47	0.86	4.28	4.25	62.5	2.04	0.33
LW-802–30			400	47,520	53.0	2.89	1170	34	0.91	2.31	9.45	70.0	2.79	0.40
LW-802–31			358	51,536	389	2.91	1417	313	1.13	31.3	78.8	70.8	3.95	1.40
LW-802–32			97.9	55,591	196	1.89	843	222	1.21	222	464	43.3	2.38	3.87
LW-802–33			354	65,479	184	2.09	1234	140	1.12	0.69	4.21	105	2.75	1.28
LW-802–34			264	62,253	175	2.19	1105	119	1.20	15.1	51.7	67.9	2.65	4.13
LW-802–35			107	53,249	125	2.46	1223	58	1.27	5.99	15.1	58.8	1.66	1.87
LW-802–36			349	41,177	41.5	1.23	641	24	0.75	1.16	5.33	44.0	1.13	0.14
LW-802–37			148	62,979	160	2.11	1045	126	1.32	2.82	8.10	53.2	2.47	3.14
LW-802–38			368	49,399	50.8	1.90	1224	38	1.44	5.14	16.6	55.0	1.89	0.59
LW-802–39			341	49,393	219	2.35	1449	155	1.28	2.98	12.4	58.4	2.99	1.24
LW-802–40			141	52,780	19.6	1.47	1674	20	0.68	3.37	12.0	62.7	1.37	1.10
LW-802–41			273	66,389	542	2.11	1361	325	1.17	bdl	0.17	77.7	4.20	2.97
LW-802–42			368	53,513	54.9	2.09	907	38	1.74	3.01	11.1	61.0	2.00	0.44
LW-802–43			399	48,887	49.8	1.35	1052	29	0.87	3.83	8.45	46.4	1.37	0.21
LW-802–44			422	57,428	182	8.21	1014	145	0.79	5.30	24.4	92.1	6.41	1.61
LW-802–45			443	60,710	159	6.90	1407	147	0.98	6.95	198	88.7	5.92	2.79
LW-802–46			458	42,305	72.8	1.69	870	49	0.80	5.18	135	49.6	2.12	0.43
LW-802–47			91.8	56,259	107	1.75	1367	91	0.94	28.9	152	59.9	2.08	3.40
LW-802–48			254	56,786	44.2	2.11	1346	47	bdl	3.49	81.0	92.0	1.84	1.39
LW-802–49			390	52,373	283	2.06	1004	229	1.39	1.03	4.89	65.2	3.78	0.59

(*continued on next page*)

Appendix 1 (*continued*)

Analysis no.	Pyrite type	Stage	Au	As	Sb	Tl	Cu	Pb	Zn	Co	Ni	Se	Ag	Bi
			~0.03*	~20 *	~0.04 *	~0.01*	~0.80 *	~0.12*	~0.45*	~0.51*	~0.59*	~0.69*	~0.01*	~0.01*
LW-803@12.6 g/t														
LW-803–1	Py1	Pre-ore	5.44	30,217	212	0.77	205	383	1.10	353	1211	25.0	3.49	5.30
LW-803–2			3.41	53,428	87.6	0.37	1062	127	0.84	28.1	526	33.0	1.07	7.45
LW-803–3			1.89	44,426	13.8	0.052	385	32	bdl	57.6	807	33.2	0.21	3.89
LW-803–4			3.47	59,779	444	1.00	665	338	0.83	128	1038	14.3	3.86	9.47
LW-803–5			1.89	60,782	33.9	0.59	927	87	0.83	159	1786	20.3	0.85	12.24
LW-803–6			28.8	57,792	164	1.04	692	131	1.89	6.83	223	25.2	1.38	5.20
LW-803–7			2.94	62,323	850	0.22	1065	67	0.58	253	2122	22.2	1.12	12.02
LW-803–8			2.19	59,465	53.9	0.23	569	55	0.68	7.19	99.6	23.8	0.84	5.53
LW-803–9			7.81	63,377	70.5	0.76	983	61	1.69	80.0	398	48.1	0.92	3.25
LW-803–10			2.20	51,906	157	0.42	538	128	0.94	98.2	822	21.6	1.78	10.70
LW-803–11			4.43	55,588	234	0.59	759	239	8.58	158	1479	18.6	2.25	11.05
LW-803–12	Py2	Ore	71.6	65,583	269	2.17	1136	166	0.64	52.2	651	34.4	3.45	7.54
LW-803–13			177	68,560	454	2.89	1776	219	1.14	10.8	211	94.0	4.60	2.78
LW-803–14			88.0	63,919	102	0.61	846	76	bdl	140	1181	40.8	1.32	4.85
LW-803–15			27.1	64,730	269	1.11	761	167	0.51	245	1133	24.6	2.58	6.06
LW-803–16			82.9	65,212	515	2.25	1230	242	0.63	34.9	203	66.1	4.53	3.52
LW-803–17			72.8	59,800	88.9	1.85	1120	47	1.05	104	1406	48.6	1.66	2.47
LW-803–18	Py3	Ore	161	67,151	161	3.64	1310	138	0.54	49.1	453	63.4	3.90	12.04
LW-803–19			396	55,126	31.1	1.39	1155	24	0.74	5.85	133	57.9	1.43	0.23
LW-803–20			355	67,348	403	5.87	1690	335	1.60	22.6	301	92.9	6.67	3.98
LW-803–21			283	43,101	75.5	1.83	1226	45	1.00	21.7	159	49.4	1.91	0.40
LW-803–22			332	58,226	48.6	0.51	768	33	0.84	0.032	0.65	67.1	0.85	0.17
LW-803–23			411	55,881	123	0.92	853	27	1.23	4.86	55.5	65.2	1.18	0.15
LW-803–24			371	55,676	1954	2.72	1428	162	0.64	2.21	25.6	78.9	4.16	3.20
LW-803–25			344	57,123	362	2.12	1055	237	1.40	2.59	13.5	66.8	5.80	0.59
LW-803–26			357	53,737	107	3.13	781	71	1.06	1.75	7.41	60.9	2.61	0.46
LW-803–27			169	63,765	1101	2.35	1722	194	0.60	7.59	104	85.0	3.37	2.94
LW-803–28			252	62,726	192	2.03	1183	214	0.67	19.4	169	70.8	2.97	2.46
LW-803–29			336	47,658	136	2.00	1070	100	0.79	1.62	17.5	47.3	2.90	0.79
LW-803–30			156	66,027	25.0	0.74	663	23	1.38	4.79	49.9	57.0	0.86	1.25
LW-803–31			392	53,546	53.9	1.05	1111	21	1.05	1.00	4.21	49.8	1.24	0.20
LW-807@13.9 g/t														
LW-807–1	Py1	Pre-ore	2.47	9603	323	1.37	137	1447	2.36	1097	4136	24.7	3.97	14.0
LW-807–2			25.5	13,466	2122	5.64	319	854	1.16	261	1005	18.1	4.48	6.63
LW-807–3			2.38	2155	119	0.25	77.2	432	2.21	30.0	106	6.17	1.46	1.89
LW-807–4			1.94	4915	248	0.38	166	1456	2.10	626	3397	21.9	3.33	22.0
LW-807–5			8.69	6382	259	0.69	155	1147	1.56	1750	5044	23.9	4.77	17.0
LW-807–6			2.17	5901	1195	0.38	148	1337	1.67	372	1833	19.4	4.24	20.3
LW-807–7			65.2	23,618	195	1.92	667	717	1.94	173	919	46.5	2.91	7.50
LW-807–8			21.5	10,330	124	2.03	293	691	1.30	129	408	15.0	2.35	8.15
LW-807–9			2.37	4246	146	0.84	91.4	641	6.93	1454	1880	24.8	2.97	15.8
LW-807–10			6.46	5206	174	0.38	72.4	422	3.94	325	935	17.6	2.48	13.4
LW-807–11	Py2	Ore	46.2	29,125	232	2.64	622	540	3.04	977	2110	44.3	3.87	13.3
LW-807–12			99.9	29,069	216	4.83	744	350	1.31	304	579	45.4	4.32	7.57
LW-807–13			82.5	25,075	163	2.71	715	629	1.57	49.1	585	48.8	2.19	1.92
LW-807–14			76.9	21,961	172	1.08	641	562	2.35	164	765	40.2	2.73	8.46
LW-807–15			63.8	32,490	284	3.19	605	521	2.30	282	734	26.4	3.40	8.73
LW-807–16			28.2	13,202	225	1.76	256	502	3.46	228	877	19.4	2.41	12.5
LW-807–17			77.3	25,188	341	5.39	657	710	1.33	942	4628	44.9	5.78	14.3
LW-807–18			33.1	15,937	267	1.21	276	648	1.01	1058	3770	31.6	4.08	14.5
LW-807–19			36.8	16,435	2899	2.68	466	1077	1.01	3203	8369	38.1	8.09	17.2
LW-807–20			57.9	17,944	160	2.07	409	502	1.58	538	913	32.3	3.56	14.1
LW-807–21			37.7	16,677	135	1.38	367	279	2.05	300	1228	22.0	2.38	7.85
LW-807–22	Py3	Ore	147	36,183	550	7.10	947	277	1.79	138	366	66.3	5.64	6.52
LW-807–23			112	29,173	269	5.06	844	340	1.26	561	1311	44.8	4.51	10.6
LW-807–24			234	43,316	243	7.52	1849	100	2.07	12.6	23.7	81.6	5.49	2.19
LW-807–25			213	38,948	303	7.39	1671	133	1.32	4.52	41.5	63.4	5.48	2.30
LW-807–26			223	41,636	240	6.89	1195	108	1.08	9.84	44.0	59.4	4.00	1.72
LW-807–27			217	44,216	210	8.09	1400	163	2.48	58.0	88.7	68.7	5.86	3.54
LW-807–28			214	33,775	105	2.77	1333	47	1.41	1.99	7.38	65.4	2.51	0.14
LW-807–29			243	43,046	152	5.52	1288	93	0.70	1.74	6.60	67.9	3.11	1.59
LW-807–30			177	41,563	264	6.91	1384	143	1.13	47.4	135	56.9	4.78	3.01
LW-807–31			91.8	61,463	284	7.93	523	612	6.33	109	463	101	4.28	7.80
LW-807–32			107	45,866	297	8.38	914	359	2.13	128	777	53.1	4.49	8.30
LW-807–33			70.3	34,731	363	6.00	516	816	1.30	206	1512	88.7	3.73	8.69
LW-807–34			172	38,218	7033	5.73	2216	157	0.86	32.0	92.2	88.5	6.21	3.12
LW-807–35			272	40,147	129	2.29	1530	33	1.43	1.84	15.3	62.9	2.49	0.11

(*continued on next page*)

Appendix 1 (*continued*)

Analysis no.	Pyrite type	Stage	Au	As	Sb	Tl	Cu	Pb	Zn	Co	Ni	Se	Ag	Bi
			~0.03*	~20 *	~0.04 *	~0.01*	~0.80 *	~0.12*	~0.45*	~0.51*	~0.59*	~0.69*	~0.01*	~0.01*
LW-807–36			215	46,379	207	16.5	1489	193	0.92	35.0	129	83.6	7.55	6.42
LW-807–37			230	41,448	53.8	4.15	1609	39	0.71	5.69	33.1	84.5	2.69	0.78
LW-807–38			163	27,673	72.1	0.68	1325	22	0.99	2.81	5.09	48.6	0.97	0.047
LW-807–39			227	33,838	111	4.39	1145	32	3.43	1.45	5.56	44.8	2.28	0.12
LW-807–40			129	33,261	79.3	2.11	769	69	1.05	32.7	81.1	50.9	1.74	1.22
LW-807–41			213	42,421	186	5.61	1534	131	1.33	35.6	205	56.9	4.55	4.07
LW-807–42			250	38,700	212	5.99	1796	105	0.99	3.33	7.61	76.9	5.05	1.85
LW-807–43			198	39,902	181	4.81	1532	86	2.42	38.7	161	55.2	3.87	2.48
LW-807–44	Py3	Ore	255	35,011	139	2.70	1205	33	1.23	1.09	7.41	67.3	2.85	0.12
LW-807–45			245	46,346	568	13.4	1725	297	0.99	24.0	95.7	74.7	10.3	8.43
LW-807–46			280	46,358	286	6.55	2050	112	1.33	20.6	45.9	70.5	5.48	2.62
LW-807–47			296	36,744	440	2.16	1573	27	3.95	3.20	8.41	49.2	2.83	0.062
LW-807–48			106	26,517	137	2.15	869	106	8.85	70.2	323	37.8	2.60	3.03
LW-807–49			297	42,379	311	5.43	1531	72	1.25	0.92	6.11	75.2	4.00	0.37
LW-807–50			298	46,864	462	6.50	1985	97	2.41	2.56	19.6	70.1	6.22	2.14
LW-807–51			275	40,466	433	5.49	1583	55	4.15	2.55	31.2	63.3	4.37	1.05
LW-807–52			261	43,081	272	7.73	1567	104	4.11	43.1	72.0	59.4	5.72	3.45
LW-807–53			210	43,399	158	6.09	1685	113	1.40	54.7	142	59.9	5.46	3.42
LW-807–54			216	43,302	251	5.91	1940	111	0.62	0.79	6.69	77.1	4.91	1.65
LW-807–55			214	38,617	180	6.48	1383	111	1.59	48.6	195	59.1	4.44	3.32
LW-807–56			288	38,106	148	5.85	1794	77	0.93	2.19	10.1	62.2	4.82	1.49
LW-807–57			251	44,462	136	4.53	1653	67	1.35	2.75	8.75	79.7	4.19	0.94
LW-807–58			232	35,830	202	7.58	1713	112	0.67	2.52	9.98	70.4	5.39	2.19
LW-807–59			216	34,251	136	2.84	1712	53	1.12	1.20	12.4	60.0	3.41	0.20
LW-807–60			224	29,608	77.0	2.39	1019	24	3.74	2.20	12.5	37.2	2.41	0.044
LW-807–61			215	44,267	1264	8.62	1819	123	0.66	17.2	45.9	82.8	6.08	2.64
LW-807–62			210	39,689	145	3.76	1457	103	1.07	41.4	104	62.3	3.96	2.15
LW-807–63			209	38,112	66.4	2.85	1365	35	0.89	2.06	11.7	55.4	2.08	0.58
LW-807–64			111	28,922	165	2.99	700	171	1.34	135	496	50.6	3.56	4.34
LW-807–65	Py3	Ore	226	33,907	81.0	3.60	1247	42	1.35	1.69	9.26	47.5	3.05	0.63
LW-807–66			123	30,656	184	2.03	775	153	4.70	51.1	251	48.0	2.71	3.38
LW-807–67			195	30,653	230	3.49	1290	109	1.09	1.63	15.3	51.9	4.39	0.23
LW-807–68			163	32,583	115	3.26	1035	147	2.96	137	332	53.1	3.13	3.50
LW-807–69			173	32,129	65.1	3.02	1112	80	0.97	58.9	232	55.6	2.86	1.99
LW-807–70			123	33,469	298	5.25	930	252	1.27	73.4	262	47.8	5.65	5.00
LW-807–71			211	46,277	583	10.7	1768	385	0.91	20.5	65.2	85.8	10.00	5.93
LW-807–72			280	36,895	148	3.64	1224	28	4.57	3.28	9.14	59.8	3.01	0.18
LW-807–73			152	36,181	142	5.65	1135	192	2.50	305	1183	57.4	5.07	7.74
LW-807–74			275	42,333	195	8.00	1791	98	2.11	1.32	5.01	72.5	7.98	2.29
LW-807–75			192	43,040	439	10.3	1495	337	1.74	147	469	67.2	7.19	10.1
LW-807–76			245	48,852	259	10.3	2060	144	1.17	5.83	21.8	89.4	6.01	3.45
LW-807–77			236	35,967	95.8	3.55	1554	37	1.00	2.53	11.4	71.3	2.52	0.68
LW-807–78			243	35,765	89.0	4.53	1649	41	0.83	1.81	14.7	51.0	3.56	0.79
LW-807–79			171	41,516	157	4.12	1355	266	1.78	92.8	323	59.0	4.23	3.77
LW-807–80			178	29,812	44.2	2.23	1196	21	0.76	0.57	1.65	47.1	1.85	0.18
LW-807–81			248	41,526	114	2.01	1587	26	1.01	2.88	22.5	70.8	1.92	0.15
LW-807–82			98.5	39,920	209	5.08	1519	421	0.95	831	1677	55.1	4.79	9.32
LW-807–83			223	45,499	176	7.18	1722	96	1.29	2.71	9.13	74.6	5.00	2.09
LW-807–84			93.3	24,990	203	3.39	872	161	0.81	96.6	301	32.6	3.64	3.21
LW-807–85			194	35,184	188	4.79	1661	105	0.99	0.45	2.12	72.8	3.51	1.77
LW-807–86			196	47,959	423	10.7	1409	265	0.96	53.4	241	65.5	7.39	5.81
LW-808@19.3 g/t														
LW-808–1	Py1	Pre-ore	6.24	9723	110	0.29	150	266	1.25	85.8	1441	27.3	1.89	1.36
LW-808–2			3.50	6032	157	0.57	75.9	517	1.97	129	2051	27.0	3.38	2.87
LW-808–3			62.9	20,821	177	2.30	604	240	1.15	118	1374	37.5	1.66	1.79
LW-808–4			21.0	18,206	113	1.46	361	313	1.03	147	1294	35.5	2.68	3.73
LW-808–5	Py2	Ore	36.8	15,475	104	3.07	361	194	1.06	83.5	1515	33.2	2.71	0.92
LW-808–6	Py3	Ore	166	35,307	110	5.80	1008	125	1.25	77.5	1031	51.4	4.12	0.68
LW-808–7			154	32,940	223	8.08	1032	144	1.57	75.5	1165	51.0	5.82	0.59
LW-808–8			173	35,574	138	7.37	922	257	1.28	55.1	465	55.0	5.66	1.36
LW-808–9			193	38,908	96.7	6.90	1215	81	1.07	41.3	441	61.5	4.96	0.46
LW-808–10			207	37,790	323	5.99	1201	127	0.74	60.4	705	47.9	5.78	0.77
LW-808–11			132	31,085	193	1.90	994	46	0.94	59.1	972	38.6	2.71	0.47
LW-808–12			102	26,055	103	1.87	652	424	1.57	71.5	973	32.7	1.86	2.38
LW-808–13			112	33,757	122	1.95	1290	58	0.76	70.5	942	46.5	2.55	0.61
LW-808–14			112	34,732	164	2.16	1219	44	0.97	75.6	693	48.4	2.34	0.88
LW-808–15			173	40,350	1259	2.56	1389	151	0.94	61.4	338	61.2	2.43	0.35
LW-808–16			190	35,277	168	4.76	1122	141	1.47	124	1288	53.6	4.59	1.41
LW-808–17			114	30,101	282	4.44	739	224	1.07	130	1338	48.4	4.07	3.03

(*continued on next page*)

Appendix 1 (*continued*)

Analysis no.	Pyrite type	Stage	Au	As	Sb	Tl	Cu	Pb	Zn	Co	Ni	Se	Ag	Bi
			~0.03*	~20 *	~0.04 *	~0.01*	~0.80 *	~0.12*	~0.45*	~0.51*	~0.59*	~0.69*	~0.01*	~0.01*
LW-812@21.6 g/t														
LW-812–1	Py1	Pre-ore	4.04	3073	3372	4.57	92.3	2466	254	657	1356	359	34.0	75.9
LW-812–2			14.2	6264	511	0.85	83.5	493	5.18	114	651	75.7	2.55	17.9
LW-812–3			44.8	20,665	368	2.47	478	375	0.99	207	947	56.7	4.00	9.51
LW-812–4			53.8	18,969	96.0	1.15	572	482	1.70	253	931	30.6	1.83	7.40
LW-812–5	Py3	Ore	163	42,496	361	2.74	1322	237	1.18	46.7	212	71.7	5.81	5.06
LW-812–6			402	47,904	179	3.01	1403	94	1.21	13.4	74.0	68.8	5.17	1.50
LW-812–7			231	39,168	214	14.4	1633	276	1.04	117	384	61.0	9.12	2.32
LW-812–8			261	51,821	608	2.31	1999	277	1.06	39.4	234	102	4.83	14.1
LW-812–9			260	53,496	254	2.93	2254	163	1.05	35.3	164	82.0	4.49	5.35
LW-812–10			93.4	23,010	183	2.47	942	222	0.80	68.5	364	45.4	3.90	6.82
LW-812–11			306	58,846	372	3.30	1959	153	12.0	10.5	57.1	164	6.14	30.8
LW-812–12			76.5	18,670	6133	9.99	442	863	1.16	127	906	621	13.4	263
LW-812–13			115	28,162	104	2.30	924	189	1.81	213	889	40.6	2.81	4.48
LW-812–14			273	39,349	257	5.37	1953	91	1.50	0.79	15.1	57.7	4.12	2.65
LW-812–15			271	40,060	123	3.78	2049	44	0.92	13.7	90.7	64.2	4.26	1.89
LW-812–16			287	50,349	1840	3.51	1955	1079	1.10	4.39	32.1	182	4.39	18.9
LW-812–17			240	41,090	146	11.3	1795	95	0.78	17.1	123	62.9	5.52	1.00
LW-812–18			363	38,494	308	2.66	1714	153	0.80	0.47	1.80	76.7	4.29	1.83
LW-812–19			137	38,520	2318	2.87	1297	235	1.94	86.6	381	208	5.54	19.2
LW-812–20			327	50,751	617	21.7	2395	2196	4.86	64.5	512	151	12.4	2.98
LW-812–21			435	55,945	1087	21.3	2810	504	1.96	45.9	371	111	11.6	2.29
LW-812–22			326	45,586	524	4.45	2317	393	1.99	11.4	118	92.9	8.69	1.71
LW-812–23			226	38,069	210	17.4	1350	137	1.04	35.2	151	61.2	12.2	1.41
LW-812–24			381	46,824	474	19.7	1981	295	0.94	77.6	279	74.4	17.5	1.94
LW-813@17.8 g/t														
LW-813–1	Py1	Pre-ore	44.2	19,476	201	1.45	921	514	1.29	454	2060	35.4	4.13	5.40
LW-813–2			9.24	7340	216	0.61	239	1299	2.21	3355	10,961	38.5	5.62	10.6
LW-813–3	Py3	Ore	94.0	24,440	285	3.11	967	568	1.50	3303	5461	47.9	5.78	14.1
LW-813–4			317	43,888	88.5	2.92	1555	47	1.57	6.21	32.3	55.3	3.25	0.25
LW-813–5			59.0	31,909	253	1.16	1352	395	1.38	86.3	647	55.0	4.34	3.79
LW-813–6			106	42,029	196	2.72	1650	377	0.82	193	1009	70.6	4.92	14.8
LW-813–7			119	38,426	414	3.75	1486	554	1.65	2341	7253	59.1	10.8	5.61
LW-813–8			307	40,966	110	2.97	1932	47	1.80	16.5	195	60.3	3.63	0.48
LW-813–9			262	46,010	92.6	4.31	2503	66	1.54	11.0	241	64.1	3.68	2.70
LW-813–10			152	45,305	136	3.16	2389	191	0.87	115	559	61.2	3.14	2.51
LW-813–11			359	46,692	178	5.21	1931	84	0.63	2.64	41.0	74.4	5.37	0.32
LW-813–12			154	39,677	85.8	4.03	1733	150	1.29	252	663	54.0	3.70	2.64
LW-813–13			272	35,749	28.2	2.81	1507	21	0.97	3.51	6.07	50.5	2.96	0.16
LW-815@7.33 g/t														
LW-815–1	Py1	Pre-ore	2.37	44,571	54.0	1.08	587	116	0.61	92.4	431	30.6	1.19	4.11
LW-815–2			2.75	47,397	76.9	0.22	369	84	1.32	264	1413	26.6	0.61	1.23
LW-815–3			4.37	12,247	114	4.01	101	696	2.91	671	1179	32.9	1.67	1.57
LW-815–4			2.66	59,904	36.4	1.01	938	94	bdl	45.0	267	30.1	0.98	3.99
LW-815–5			3.79	49,347	31.8	0.34	496	160	0.47	263	866	35.6	0.68	1.95
LW-815–6			7.05	44,107	32.6	0.25	405	150	1.16	39.2	572	34.7	0.35	1.02
LW-815–7			2.88	30,675	2.32	0.016	127	13	1.09	53.7	207	37.8	0.025	0.48
LW-815–8			2.66	21,638	41.9	0.074	140	325	1.16	436	666	35.4	0.57	0.64
LW-815–9			2.21	45,495	49.0	0.29	460	243	1.30	283	1856	22.9	0.68	3.37
LW-815–10			3.27	61,938	42.8	0.62	480	43	1.18	3.05	89.3	22.2	0.67	0.77
LW-815–11			4.30	60,462	7.40	0.26	841	12	1.27	5.82	54.8	32.8	0.19	0.48
LW-815–12			7.03	36,322	99.0	0.39	478	435	0.90	347	1264	66.6	1.26	3.58
LW-815–13			14.2	22,771	169	3.66	188	220	1.10	79.0	442	46.0	4.97	4.54
LW-815–14			6.95	40,126	22.3	0.44	652	71	1.14	111	605	40.6	0.59	3.01
LW-815–15			4.55	50,870	63.9	0.40	649	163	1.13	107	583	27.3	0.57	1.54
LW-815–16			4.18	5469	87.1	0.51	59.7	576	1.00	709	826	7.98	1.38	0.71
LW-815–17			8.45	38,783	88.7	1.05	530	310	1.13	152	620	40.5	1.34	6.03
LW-815–18			4.33	53,659	33.4	0.65	818	130	0.59	41.4	321	44.2	0.97	4.13
LW-815–19	Py2	Ore	20.2	61,553	53.2	3.81	951	73	1.47	16.6	98.8	42.3	1.23	1.47
LW-815–20			11.0	59,120	24.5	1.01	1306	78	1.06	9.47	70.6	34.0	3.72	3.67
LW-815–21			41.2	51,631	76.3	2.23	1405	81	0.79	1.28	46.7	64.2	2.04	1.97
LW-815–22			5.66	58,226	32.6	1.40	772	32	1.07	5.51	59.7	44.0	0.69	0.64
LW-815–23			66.2	54,994	28.1	1.12	1050	30	1.04	1.64	51.4	55.7	1.05	0.76
LW-815–24			49.4	64,180	15.7	2.37	885	30	0.83	10.4	22.3	38.0	0.74	1.09
LW-815–25			54.9	57,016	33.2	0.77	658	39	0.69	10.2	106	35.1	0.80	0.80
LW-815–26			98.4	60,105	22.3	0.81	987	32	0.88	6.98	57.0	50.7	1.14	0.91

(*continued on next page*)

Appendix 1 (*continued*)

Analysis no.	Pyrite type	Stage	Au	As	Sb	Tl	Cu	Pb	Zn	Co	Ni	Se	Ag	Bi
			~0.03*	~20 *	~0.04 *	~0.01*	~0.80 *	~0.12*	~0.45*	~0.51*	~0.59*	~0.69*	~0.01*	~0.01*
LW-815–27			6.20	63,224	23.3	2.33	567	33	bdl	32.6	212	25.5	0.55	1.02
LW-815–28			13.4	61,019	9.82	0.42	761	31	3.27	20.6	290	26.5	0.41	2.46
LW-815–29			75.7	57,179	52.4	1.62	1090	55	0.76	14.0	147	63.3	1.65	1.36
LW-815–30			17.6	65,084	21.8	0.73	1257	29	0.78	5.47	71.7	38.5	0.70	0.93
LW-815–31	Py3	Ore	304	57,700	56.5	2.58	1040	50	1.12	4.47	119	75.9	3.23	1.63
LW-815–32			134	61,981	48.5	1.94	924	47	0.73	5.67	54.2	51.4	2.24	0.97
LW-815–33			463	55,470	102	2.40	877	88	0.86	0.056	245	88.6	2.85	0.66
LW-815–34			475	51,768	31.5	3.38	987	23	0.99	6.73	62.7	75.7	2.81	0.27
LW-815–35			441	58,471	32.9	1.67	771	27	1.06	4.25	159	82.3	2.06	0.45
LW-815–36			386	45,561	43.0	3.19	1097	28	1.55	7.10	47.7	63.3	3.09	0.21
LW-815–37			239	64,134	141	4.22	946	113	1.12	16.8	83.3	74.2	3.01	2.01
LW-815–38			221	56,062	76.6	2.71	1015	87	1.15	2.62	58.6	88.9	3.49	2.77
LW-815–39			411	61,126	27.9	1.71	1348	20	1.30	0.34	1.88	75.6	2.03	0.15
LW-815–40			152	52,718	9.45	0.79	1076	14	1.47	3.83	23.1	64.5	0.84	0.46
LW-815–41			201	42,211	11.8	1.06	727	9	1.39	0.080	5.22	66.9	0.52	0.12
LW-815–42			251	40,282	36.8	2.19	1231	31	1.00	3.55	86.8	59.7	2.24	0.34
LW-815–43			159	36,995	78.0	1.63	690	51	1.40	0.73	4.91	59.2	1.42	0.34
LW-815–44			296	56,329	65.0	4.02	1096	55	1.11	7.57	66.1	71.5	2.59	2.44
LW-815–45			377	58,687	17.9	1.43	845	17	0.99	14.3	80.1	90.2	2.16	0.46
LW-815–46			128	53,601	12.9	0.91	866	10	1.40	5.39	26.9	53.7	1.22	0.17
LW-815–47	Py3	Ore	218	59,741	38.5	1.77	889	37	0.52	5.70	25.5	76.4	1.73	0.68
LW-815–48			251	61,073	39.8	1.62	1056	46	1.08	2.04	35.5	78.8	1.64	1.42
LW-815–49			103	62,981	46.8	1.47	664	49	0.79	2.02	26.0	44.6	1.50	1.02
LW-815–50			411	44,104	38.6	3.22	852	30	1.39	2.31	67.8	58.7	3.35	0.36
LW-815–51			166	60,061	18.6	1.00	666	23	0.79	9.95	120	67.8	0.85	0.38
LW-815–52			116	62,922	41.4	1.73	870	44	0.86	0.22	12.6	50.1	1.45	0.96
LW-815–53			231	58,987	35.5	1.70	1007	30	0.64	11.6	64.6	60.3	1.76	0.74
LW-815–54			310	36,599	23.5	1.68	917	17	0.63	0.64	29.9	53.8	1.73	0.20
LW-815–55			264	52,467	118	4.38	766	97	0.96	2.81	65.6	107	3.16	1.57
LW-815–56			116	61,847	24.9	0.98	901	32	1.15	7.18	39.8	66.1	1.34	1.25
LW-815–57			231	49,953	106	3.85	697	86	0.55	0.70	14.8	82.8	3.22	1.52
LW-815–58			186	45,439	150	3.83	846	130	0.99	7.44	27.6	54.7	4.89	1.70
LW-815–59			285	52,618	36.4	1.56	1048	27	1.03	0.77	8.11	80.2	2.25	0.51
LW-815–60			284	44,061	36.9	1.48	902	35	1.26	0.44	4.89	66.7	1.72	0.28
LW-815–61			262	45,198	73.9	3.01	1029	55	1.58	2.20	135	74.8	3.04	0.59
LW-815–62			112	55,301	35.9	0.72	989	30	1.18	19.5	131	38.8	1.09	0.56
LW-815–63			369	47,290	21.0	1.34	947	11	0.73	4.64	72.1	83.2	1.54	0.18
LW-815–64			429	58,994	97.4	2.99	605	87	1.20	5.22	35.8	115	4.01	1.38
LW-815–65			102	61,348	12.3	1.58	1274	23	2.03	2.60	76.0	79.4	0.63	1.02
LW-815–66			301	52,818	45.5	2.77	1088	36	0.66	39.3	302	70.1	2.47	0.76
LW-815–67			303	58,858	42.2	1.44	881	32	0.87	4.05	79.1	86.7	1.81	0.74
LW-815–68	Py3	Ore	164	37,578	123	3.91	1307	88	1.24	0.20	258	62.1	3.06	1.15
LW-815–69			492	57,986	54.0	1.45	1010	45	1.21	0.25	11.9	83.0	2.70	0.27

Abbreviations: bdl = below detection limit, Py 1 = Pre-ore pyrite 1, Py 2 = Ore pyrite 2 (inner rim), Py 3 = Ore pyrite 3 (outer rim).
*Value listed below the element is the detection limit (in ppm).

Appendix 2
In situ SIMS multiple S isotope compositions of pyrites from the Linwang deposit.

Analysis no.	Type	Stage	$\delta^{33}S$ (‰)	2SE	$\delta^{34}S$ (‰)	2SE	$\Delta^{33}S$ (‰)	2SE
LW-808@19.3 g/t								
LW-808–1	Py1	Pre-ore	3.38	0.08	6.77	0.13	−0.10	0.06
LW-808–2			1.81	0.08	3.54	0.13	−0.01	0.06
LW-808–3			2.41	0.08	4.86	0.13	−0.09	0.06
LW-808–4			2.28	0.08	4.53	0.13	−0.05	0.06
LW-808–5			2.29	0.08	4.64	0.13	−0.09	0.06
LW-808–6			3.16	0.08	6.09	0.13	0.02	0.06
LW-808–7			2.66	0.08	5.39	0.13	−0.12	0.06
LW-808–8			3.06	0.08	5.93	0.13	0.01	0.06
LW-808–9			3.03	0.08	5.85	0.13	0.02	0.06
LW-808–10			2.88	0.08	5.78	0.13	−0.09	0.06
LW-808–11			3.21	0.08	6.44	0.13	−0.10	0.06
LW-808–12			3.32	0.08	6.32	0.13	0.07	0.06
LW-808–13			3.12	0.08	6.17	0.13	−0.05	0.06
LW-808–14			3.18	0.08	6.12	0.13	0.03	0.06
LW-808–15			2.97	0.08	5.99	0.13	−0.11	0.06
LW-808–16			2.71	0.08	5.34	0.13	−0.03	0.06
LW-808–17			3.41	0.08	6.66	0.13	−0.01	0.06

(*continued on next page*)

Appendix 2 (*continued*)

Analysis no.	Type	Stage	$\delta^{33}S$ (‰)	2SE	$\delta^{34}S$ (‰)	2SE	$\Delta^{33}S$ (‰)	2SE
LW-808–18			3.19	0.08	6.25	0.13	−0.02	0.06
LW-808–19			2.12	0.08	4.20	0.13	−0.03	0.06
LW-808–20			3.13	0.08	6.01	0.13	0.04	0.06
LW-808–21			3.51	0.08	6.99	0.13	−0.09	0.06
LW-808–22			3.49	0.08	6.76	0.13	0.01	0.06
LW-808–23			3.42	0.08	6.72	0.13	−0.04	0.06
LW-808–24	Py2	Ore	1.97	0.08	3.78	0.13	0.03	0.06
LW-808–25	Py3	Ore	2.07	0.08	4.08	0.13	−0.03	0.06
LW-808–26			2.11	0.08	4.13	0.13	−0.02	0.06
LW-808–27			2.10	0.08	4.17	0.13	−0.05	0.06
LW-808–28			2.12	0.08	4.23	0.13	−0.06	0.06
LW-808–29			2.05	0.08	4.04	0.13	−0.02	0.06
LW-808–30			2.30	0.08	4.55	0.13	−0.04	0.06
LW-808–31			2.21	0.08	4.39	0.13	−0.05	0.06
LW-808–32			2.39	0.08	4.78	0.13	−0.07	0.06
LW-808–33			2.02	0.08	4.10	0.13	−0.09	0.06
LW-808–34			2.13	0.08	4.50	0.13	−0.18	0.06
LW-808–35			2.76	0.08	5.42	0.13	−0.03	0.06
LW-808–36			2.34	0.08	4.81	0.13	−0.13	0.06
LW-808–37			2.10	0.08	4.24	0.13	−0.08	0.06
LW-808–38			2.23	0.08	4.41	0.13	−0.04	0.06
LW-808–39	Py 3	Ore	2.09	0.08	4.11	0.13	−0.02	0.06
LW-808–40			2.05	0.08	3.93	0.13	0.03	0.06
LW-808–41			2.24	0.08	4.56	0.13	−0.11	0.06
LW-808–42			2.29	0.08	4.34	0.13	0.05	0.06
LW-808–43			3.10	0.08	6.08	0.13	−0.03	0.06
LW-808–44			2.01	0.08	4.13	0.13	−0.12	0.06
LW-808–45			2.34	0.08	4.62	0.13	−0.04	0.06
LW-808–46			2.13	0.08	4.28	0.13	−0.07	0.06
LW-815@7.33g/t								
LW-815–1	Py1	Pre-ore	2.05	0.08	4.03	0.13	−0.03	0.06
LW-815–2			2.25	0.08	4.26	0.13	0.06	0.06
LW-815–3			2.47	0.08	4.72	0.13	0.04	0.06
LW-815–4			3.89	0.08	7.65	0.13	−0.04	0.06
LW-815–5			3.20	0.08	6.24	0.13	0.00	0.06
LW-815–6			2.31	0.08	4.31	0.13	0.09	0.06
LW-815–7			1.49	0.08	2.88	0.13	0.00	0.06
LW-815–8			2.38	0.08	4.46	0.13	0.09	0.06
LW-815–9			2.53	0.08	4.94	0.13	−0.01	0.06
LW-815–10			2.00	0.08	3.87	0.13	0.01	0.06
LW-815–11			3.74	0.08	7.24	0.13	0.01	0.06
LW-815–12			2.31	0.08	4.42	0.13	0.03	0.06
LW-815–13			2.11	0.08	4.13	0.13	−0.01	0.06
LW-815–14			2.53	0.08	4.88	0.13	0.02	0.06
LW-815–15			2.16	0.08	4.10	0.13	0.06	0.06
LW-815–16			3.53	0.08	6.61	0.13	0.13	0.06
LW-815–17			1.82	0.08	3.38	0.13	0.08	0.06
LW-815–18			2.40	0.08	4.57	0.13	0.05	0.06
LW-815–19			1.89	0.08	3.53	0.13	0.07	0.06
LW-815–20			1.59	0.08	3.06	0.13	0.01	0.06
LW-815–21			2.56	0.08	4.87	0.13	0.05	0.06
LW-815–22			1.99	0.08	3.77	0.13	0.05	0.06
LW-815–23			1.49	0.08	2.73	0.13	0.08	0.06
LW-815–24			1.79	0.08	3.44	0.13	0.02	0.06
LW-815–25			2.45	0.08	4.56	0.13	0.11	0.06
LW-815–26	Py2	Ore	2.57	0.08	5.11	0.13	−0.05	0.06
LW-815–27			2.89	0.08	5.53	0.13	0.04	0.06
LW-815–28			2.46	0.08	4.77	0.13	0.01	0.06
LW-815–29			2.63	0.08	5.08	0.13	0.02	0.06
LW-815–30			2.83	0.08	5.46	0.13	0.02	0.06
LW-815–31			2.44	0.08	4.65	0.13	0.05	0.06
LW-815–32			2.48	0.08	4.75	0.13	0.04	0.06
LW-815–33			2.74	0.08	5.21	0.13	0.05	0.06
LW-815–34			2.66	0.08	5.17	0.13	0.00	0.06
LW-815–35			2.64	0.08	5.17	0.13	−0.02	0.06
LW-815–36			2.64	0.08	5.09	0.13	0.02	0.06
LW-815–37			2.60	0.08	5.03	0.13	0.02	0.06
LW-815–38			2.92	0.08	5.60	0.13	0.04	0.06
LW-815–39			2.49	0.08	4.86	0.13	−0.01	0.06
LW-815–40			3.11	0.08	5.85	0.13	0.10	0.06
LW-815–41			2.70	0.08	5.32	0.13	−0.04	0.06
LW-815–42			2.28	0.08	4.15	0.13	0.15	0.06
LW-815–43			2.26	0.08	4.37	0.13	0.01	0.06
LW-815–44			2.40	0.08	4.58	0.13	0.05	0.06
LW-815–45			2.46	0.08	4.85	0.13	−0.03	0.06

(*continued on next page*)

Appendix 2 (*continued*)

Analysis no.	Type	Stage	$\delta^{33}S$ (‰)	2SE	$\delta^{34}S$ (‰)	2SE	$\Delta^{33}S$ (‰)	2SE
LW-815–46			2.27	0.08	4.24	0.13	0.09	0.06
LW-815–47			2.69	0.08	5.16	0.13	0.04	0.06
LW-815–48			2.29	0.08	4.32	0.13	0.07	0.06
LW-815–49			1.86	0.08	3.51	0.13	0.05	0.06
LW-815–50			2.31	0.08	4.48	0.13	0.00	0.06
LW-815–51			2.62	0.08	5.04	0.13	0.03	0.06
LW-815–52			2.28	0.08	4.39	0.13	0.02	0.06
LW-815–53	Py3	Ore	2.43	0.08	4.58	0.13	0.07	0.06
LW-815–54			2.02	0.08	3.80	0.13	0.06	0.06
LW-815–55			3.08	0.08	5.96	0.13	0.02	0.06
LW-815–56			2.16	0.08	4.12	0.13	0.04	0.06
LW-815–57			2.59	0.08	5.02	0.13	0.00	0.06
LW-815–58			2.00	0.08	3.81	0.13	0.04	0.06
LW-815–59			2.72	0.08	5.28	0.13	0.01	0.06
LW-815–60			2.12	0.08	4.14	0.13	−0.01	0.06
LW-815–61			2.43	0.08	4.71	0.13	0.00	0.06
LW-815–62			2.47	0.08	4.78	0.13	0.01	0.06
LW-815–63			2.30	0.08	4.44	0.13	0.02	0.06
LW-815–64			2.39	0.08	4.65	0.13	0.00	0.06
LW-815–65			2.27	0.08	4.38	0.13	0.02	0.06
LW-815–66			3.07	0.08	5.88	0.13	0.04	0.06
LW-815–67			2.10	0.08	4.02	0.13	0.04	0.06
LW-815–68			2.87	0.08	5.41	0.13	0.09	0.06
LW-815–69			2.10	0.08	4.06	0.13	0.01	0.06
LW-815–70	Py 3	Ore	2.23	0.08	4.38	0.13	−0.02	0.06
LW-815–71			2.21	0.08	4.01	0.13	0.14	0.06
LW-815–72			2.18	0.08	4.30	0.13	−0.03	0.06
LW-815–73			2.47	0.08	4.84	0.13	−0.02	0.06
LW-815–74			2.43	0.08	4.76	0.13	−0.02	0.06
LW-815–75			2.44	0.08	4.75	0.13	−0.01	0.06

Abbreviations: Py1 = Pre-ore pyrite 1, Py2 = Ore pyrite 2 (inner rim), Py3 = Ore pyrite 3 (outer rim). $\Delta^{33}S = \delta^{33}S - (1000\times((1+\delta^{34}S/1000)^{0.515} - 1))$

References

Agangi, A., Hofmann, A., Eickmann, B., Marin-Carbonne, J., Reddy, S.M., 2016. An atmospheric source of S in Mesoarchaean structurally-controlled gold mineralisation of the Barberton Greenstone Belt. Precambrian Res. 285, 10–20.

Barker, S.L.L., Hickey, K.A., Cline, J.S., Dipple, G.M., Kilburn, M.R., Vaughan, J.R., Longo, A.A., 2009. Uncloaking invisible gold: use of nanoSIMS to evaluate gold, trace elements, and sulfur isotopes in pyrite from Carlin-type gold deposits. Econ. Geol. 104, 897–904.

Bekker, A., Holland, H.D., Wang, P.L., Rumble III, D., Stein, H.J., Hannah, J.L., Coetzee, L.L., Beukes, N.J., 2004. Dating the rise of atmospheric oxygen. Nature. 427, 117–120.

Cabral, R.A., Jackson, M.G., Rose-Koga, E.F., Koga, K.T., Whitehouse, M.J., Antonelli, M. A., Farquhar, J., Day, J.M.D., Hauri, E.H., 2013. Anomalous sulphur isotopes in plume lavas reveal deep mantle storage of Archean crust. Nature. 496, 490–493.

Cai, J.X., Zhang, K.J., 2009. A new model for the Indochina and South China collision during the Late Permian to the Middle Triassic. Tectono-physics. 467, 35–43.

Chen, M.H., Huang, Q.W., Li, J.X., Jiang, B.C., Zhang, C.M., 2010. Structure analysis and structural metallogenies of the Linwang gold deposit, Leye, Guangxi, China. Geotectonica Metall. 34, 349–361 (in Chinese with English abstract).

Chen, M.H., Zhang, Y., Meng, Y.Y., Lu, G., Liu, S.Q., 2014. Determination of upper limit of metallogenic epoch of Liaotun gold deposit in western Guangxi and its implications for chronology of Carlin-type gold deposits in Yunnan-Guizhou-Guangxi "Golden Triangle" area. Mineral Deposits 33, 1–13 (in Chinese with English abstract).

Chen, M.H., Bagas, L., Liao, X., Zhang, Z.Q., Li, Q.L., 2019. Hydrothermal apatite SIMS Th-Pb dating, constraints on the timing of low-temperature hydrothermal Au deposit in Nibao, SW China. Lithos 324–325, 418–428.

Cline, J.S., 2018. Nevada's Carlin-type gold deposits: what we've learned during the past 10 to 15 years. Soc. Econ. Geol. 20, 7–37.

Cline, J.S., Hofstra, A.H., Muntean, J.L., Tosdal, R.M., Hickey, K.A., 2005. Carlin-type gold deposits in Nevada: critical geologic characteristics and viable models. Econ. Geol. 100th Anniversary 451–484.

Dong, W.D., 2017. Geochemistry of diabase-hosted gold deposits along the southern margin of Youjiang basin. Unpublished Ph.D. dissertation, Guiyang, China, Institute of Geochemistry, Chinese Academy of Sciences (in Chinese with English abstract).

Du, Y.S., Huang, H., Yang, J.H., Huang, H.W., Tao, P., Huang, Z.Q., Hu, L.S., Xie, C.X., 2013. The basin translation from late Paleozoic to Triassic of the Youjiang basin and its tectonic signification. Geol. Rev. 59, 1–11 (in Chinese with English abstract).

Du, B.S., Shen, J.F., Santosh, M., Liu, H.M., Liu, J.J., Wang, Y.H., Xu, K.X., 2021. Textural, compositional and isotopic characteristics of pyrite from the Zaozigou gold deposit in West Qinling, China: implications for gold metallogeny. Ore Geol. Rev. 130, 103917.

Emsbo, P., Hofstra, A.H., Lauha, E.A., Griffin, G.L., Hutchinson, R.W., 2003. Origin of high-grade gold ore, source of ore fluid components, and genesis of the Meikle and neighboring Carlin-type deposits, northern Carlin trend, Nevada. Econ. Geol. 98, 1069–1100.

Farquhar, J., Wing, B.A., 2003. Multiple sulfur isotopes and the evolution of the atmosphere. Earth Planet. Sci. Lett. 213, 1–13.

Farquhar, J., Bao, H.M., Thiemens, M., 2000. Atmospheric influence of earth's earliest sulfur cycle. Science 289, 756–759.

Feng, L., Li, Y., 2019. Comparative partitioning of Re and Mo between sulfide phases and silicate melt and implications for the behavior of Re during magmatic processes. Earth Planet. Sci. Lett. 517, 14–25.

Gao, W., Hu, R.Z., Hofstra, A.H., Li, Q.L., Zhu, J.J., Peng, K.Q., Mu, L., Huang, Y., Ma, J. W., Zhao, Q., 2021. U-Pb dating on hydrothermal rutile and monazite from the Badu gold deposit supports an early Cretaceous age for Carlin-type gold mineralization in the Youjiang basin, Southwestern China. Econ. Geol. 116, 1355–1385.

Gao, W., 2018. Geochronology and geodynamics of Carlin-type gold deposit in the Youjiang basin (NW Guangxi). Unpublished Ph.D. dissertation, Guiyang, China, Institute of Geochemistry, Chinese Academy of Sciences (in Chinese with English abstract).

Gilbert, S.E., Danyushevsky, L.V., Rodemann, T., Shimizu, N., Guienko, A., Meffre, S., Thomas, H., Large, R.R., Death, D., 2014. Optimisation of laser parameters for the analysis of sulphur isotopes in sulphide minerals by laser ablation ICP-MS. J. Anal. At. Spectrom. 29, 1042–1051.

Gopon, P., Douglas, J.O., Auger, M.A., Hansen, L., Wade, J., Cline, J.S., Robb, L.J., Moody, M.P., 2019. A nanoscale investigation of Carlin-type gold deposits: an atom-scale elemental and isotopic perspective. Econ. Geol. 114, 1123–1133.

Gregory, D.D., Large, R.R., Halpin, J.A., Baturina, E.L., Lyons, T.W., Wu, S., Danyushevsky, L., Sack, P.J., Chappaz, A., Maslennikov, V.V., Bull, S.W., 2015. Trace element content of sedimentary pyrite in black shales. Econ. Geol. 110, 1389–1410.

Gregory, D.D., Large, R.R., Bath, A.B., Steadman, J.A., Wu, S., Danyushevsky, L., Bull, S. W., Holden, P., Ireland, T.R., 2016. Trace element content of pyrite from the Kapai Slate, St. Ives Gold District, Western Australia. Econ. Geol. 111, 1297–1320.

Groves, D.I., Goldfarb, R.J., Gebre-Mariam, M., Hagemann, S.G., Robert, F., 1998. Orogenic gold deposits: a proposed classification in the context of their crustal distribution and relationships to other gold deposit types. Ore Geol. Rev. 13, 7–27.

Gu, X.X., Zhang, Y.M., Li, B.H., Dong, S.Y., Xue, C.J., Fu, S.H., 2012. Hydrocarbon- and ore-bearing basinal fluids: a possible link between gold mineralization and hydrocarbon accumulation in the Youjiang basin, South China. Miner. Deposita. 47, 663–682.

Hofstra, A.H., Cline, J.S., 2000. Characteristics and models for Carlin-type gold deposits. Soc. Econ. Geol. 13, 163–220.

Hofstra, A.H., Leventhal, J.S., Northrop, H.R., Landis, G.P., Rye, R.O., Birak, D.J., Dahl, A.R., 1991. Genesis of sediment-hosted disseminated gold deposits by fluid mixing and sulfidation: chemical-reaction-path modeling of ore-depositional processes documented in the Jerritt Canyon district, Nevada. Geology. 19, 36–40.

Hofstra, A.H., Christiansen, W.D., Zohar, P.B., Tousignant, G., 2011. Lithogeochemistry of the Devonian Popovich Formation in the northern Carlin Trend, Nevada. In: Steininger, R., Pennell, B. (Eds.), Great Basin evolution and metallogeny: 2010 Symposium proceedings. Nevada, Geological Society of Nevada, Reno, pp. 63–96.

Hou, L., Peng, H.J., Ding, J., Zhang, J.R., Zhu, S.B., Wu, S.Y., Wu, Y., Ouyang, H.G., 2016. Textures and in situ chemical and isotopic analyses of pyrite, Huijiabao trend, Youjiang basin, China: implications for paragenesis and source of sulfur. Econ. Geol. 111, 331–353.
Hu, R.Z., Su, W.C., Bi, X.W., Tu, G.Z., Hofstra, A.H., 2002. Geology and geochemistry of Carlin-type gold deposits in China. Miner. Deposita. 37, 378–392.
Hu, R.Z., Fu, S.L., Huang, Y., Zhou, M.F., Fu, S.H., Zhao, C.H., Wang, Y.J., Bi, X.W., Xiao, J.F., 2017. The giant South China Mesozoic low-temperature metallogenic domain: reviews and a new geodynamic model. J. Asian Earth Sci. 137, 9–34.
Hu, X.L., Gong, Y.J., Zeng, G.P., Zhang, Z.J., Wang, J., Yao, S.Z., 2018. Multistage pyrite in the Getang sediment-hosted disseminated gold deposit, southwestern Guizhou Province, China: insights from textures and in situ chemical and sulfur isotopic analyses. Ore Geol. Rev. 99, 1–16.
Huang, K.N., 1986. The Petrological and geochemical characteristics and the tectonic setting of the Emeishan basalts in Kangdian Craton and adjacent areas. Unpublished Ph.D. dissertation. Institute of Geology, Chinese Academy of Geological Sciences, Beijing, China (in Chinese with English abstract).
Huang, Y., 2019. Mineralization age and material source of the Carlin-type gold deposits in Southwestern Guizhou. Unpublished Ph.D. dissertation, Guiyang, China, Institute of Geochemistry, Chinese Academy of Sciences (in Chinese with English abstract).
Hulston, J.R., Thode, H.G., 1965. Variations in ^{33}S, ^{34}S and ^{36}S contents of meteorites and their relation to chemical and nuclear effects. J. Geophys. Res. 70, 3475–3484.
Ilchik, R.P., Barton, M.D., 1997. An amagmatic origin of Carlin-type gold deposits. Econ. Geol. 92, 269–288.
Jin, X.Y., 2017. Geology, mineralization and genesis of the Nibao, Shuiyindong and Yata gold deposit in SW Guizhou Province, China. Unpublished Ph.D. dissertation, Wuhan, China, China University of Geosciences (in Chinese with English abstract).
Johnston, D.T., 2011. Multiple sulfur isotopes and the evolution of Earth's surface sulfur cycle. Earth Sci. Rev. 106, 161–183.
Kesler, S.E., Fortuna, J., Ye, Z., Alt, J.C., Core, D.P., Zohar, P., Borhauer, J., Chryssoulis, S.L., 2003. Evaluation of the role of sulfidation in deposition of gold, Screamer section of the Betze-Post Carlin-type deposit, Nevada. Econ. Geol. 98, 1137–1157.
Kesler, S.E., Riciputi, L.C., Ye, Z.J., 2005. Evidence for a magmatic origin for Carlin-type gold deposits: isotopic composition of sulfur in the Betze-Post-Screamer deposit, Nevada, USA. Miner. Deposita. 40, 127–136.
Kusebauch, C., Oelze, M., Gleeson, S., 2018. Partitioning of arsenic between hydrothermal fluid and pyrite during experimental siderite replacement. Chem. Geol. 500, 136–147.
Kusebauch, C., Gleeson, S., Oelze, M., 2019. Coupled partitioning of Au and As into pyrite controls formation of giant Au deposits. Sci. Adv. 5, 1–8.
LaFlamme, C., Sugiono, D., Thebaud, N., Caruso, S., Fiorentini, M., Selvaraja, V., Jeon, H., Voute, F., Martin, L., 2018. Multiple sulfur isotopes monitor fluid evolution of an Archean orogenic gold deposit. Geochim. Cosmochim. Acta. 222, 436–446.
Lai, C.K., Meffre, S., Crawford, A.J., Zaw, K., Xue, C.D., Halpin, J.A., 2014. The western Ailaoshan volcanic belts and their SE Asia connection: a new tectonic model for the eastern Indochina block. Gondwana Res. 26, 52–74.
Large, R.R., Maslennikov, V.V., Robert, F., Danyushevsky, L.V., Chang, Z.S., 2007. Multistage sedimentary and metamorphic origin of pyrite and gold in the giant Sukhoi Log deposit, Lena gold province, Russia. Econ. Geol. 102, 1233–1267.
Large, R.R., Danyushevsky, L., Hollit, C., Maslennikov, V., Meffre, S., Gilbert, S., Bull, S., Scott, R., Emsbo, P., Thomas, H., Singh, B., Foster, J., 2009. Gold and trace element zonation in pyrite using a laser imaging technique: implications for the timing of gold in orogenic and Carlin-style sediment-hosted deposits. Econ. Geol. 104, 635–668.
Large, R.R., Bull, S.W., Maslennikov, V.V., 2011. A carbonaceous sedimentary source-rock model for Carlin-type and orogenic gold deposits. Econ. Geol. 106, 331–358.
Li, X.H., Bai, L.A., Yue, Z.H., Pang, B.C., Wei, D.T., 2021. Mineralization processes involved in the formation of the Jinya Carlin-type Au deposit, northwestern Guangxi, China: evidence from in situ trace element and S isotope geochemistry of Au-bearing zoned pyrite. Ore Geol. Rev. 138, 104367.
Li, J.X., Hu, R.Z., Zhao, C.H., Zhu, J.J., Huang, Y., Gao, W., Li, J.W., Zhuo, Y.Z., 2020. Sulfur isotope and trace element compositions of pyrite determined by NanoSIMS and LA-ICP-MS: new constraints on the genesis of the Shuiyindong Carlin-like gold deposit in SW China. Miner. Deposita. 55, 1279–1298.
Li, Z.X., Li, X.H., 2007. Formation of the 1300-km-wide intracontinental orogen and postorogenic magmatic province in Mesozoic South China: a flat-slab subduction model. Geology. 35, 179–182.
Li, R.C., Xia, X.P., Yang, S.H., Chen, H.Y., Yang, Q., 2018. Off-mount calibration and one new potential pyrrhotite reference material for sulfur isotope measurement by secondary ion mass spectrometry. Geostand. Geoanal. Res. 43, 177–187.
Liang, J.L., Li, J., Liu, X.M., Zhai, W., Huang, Y., Zhao, J., Sun, W.D., Song, M.C., Li, J.Z., 2020. Multiple element mapping and in-situ S isotopes of Au-carrying pyrite of Shuiyindong gold deposit, southwestern China using nanoSIMS: constraints on Au sources, ore fluids, and mineralization processes. Ore Geol. Rev. 123, 103576.
Liang, Q.L., Xie, Z.J., Song, X.Y., Wirth, R., Xia, Y., Cline, J.S., 2021. Evolution of invisible Au in arsenian pyrite in Carlin-type Au deposits. Econ. Geol. 116, 515–526.
Lin, S.R., Hu, K., Cao, J., Bai, T., Liu, Y., Han, S.C., 2021. An in situ sulfur isotopic investigation of the origin of Carlin-type gold deposits in Youjiang Basin, southwest China. Ore Geol. Rev. 134, 104187.
Liu, Y.S., Hu, Z.C., Gao, S., Günther, D., Xu, J., Gao, C.G., Chen, H.H., 2008. In situ analysis of major and trace elements of anhydrous minerals by LA-ICP-MS without applying an internal standard. Chem. Geol. 257, 34–43.
Liu, S., Su, W.C., Hu, R.Z., Feng, C.X., Gao, S., Coulson, I.M., Wang, T., Feng, G.Y., Tao, Y., Xia, Y., 2010. Geochronological and geochemical constraints on the petrogenesis of alkaline ultramafic dykes from southwest Guizhou Province, SW China. Lithos 114, 253–264.
Luo, W., Liang, G.H., Xie, X.Y., Ma, K.Z., 2019. Study on fluid inclusions of Linwang gold deposit in Leye County, Guangxi. Miner. Resour. Geol. 33, 606–612 (in Chinese with English abstract).
Masterson, A.L., Farquhar, J., Wing, B.A., 2011. Sulfur mass-independent fractionation patterns in the broadband UV photolysis of sulfur dioxide: pressure and third body effects. Earth Planet. Sci. Lett. 306, 253–260.
Muntean, J.L., Cline, J.S., 2018. Diversity of Carlin-type gold deposits. Soc. Econ. Geol. 20, 1–5.
Muntean, J.L., Cline, J.S., Simon, A.C., Longo, A.A., 2011. Magmatic-hydrothermal origin of Nevada's Carlin-type gold deposits. Nat. Geosci. 4, 122–127.
Nevolko, P.A., Tran, T.H., Yudin, D.S., Ngo, T.P., 2017. Ar-Ar ages of gold deposits in the Song Hien domain (NE Vietnam): tectonic settings and comparison with Golden Triangle in China in terms of a single metallogenic province. Ore Geol. Rev. 89, 544–556.
Ohmoto, H., 1972. Systematics of sulfur and carbon isotopes in hydrothermal ore deposits. Econ. Geol. 67, 551–578.
Ohmoto, H., Watanabe, Y., Ikemi, H., Poulson, S.R., Taylor, B.E., 2007. Sulphur isotope evidence for an oxic Archaean atmosphere. Nature. 442, 908–911.
Ono, S., Eigenbrode, J.L., Pavlov, A.A., Kharecha, P., Rumble, D., Kasting, J.F., Freeman, K.H., 2003. New insights into Archean sulfur cycle from mass-independent sulfur isotope records from the Hamersley Basin, Australia. Earth Planet. Sci. Lett. 213, 15–30.
Palenik, C.S., Utsunomiya, S., Reich, M., Kesler, S.E., Wang, L.M., Ewing, R.C., 2004. "Invisible" gold revealed: direct imaging of gold nanoparticles in a Carlin-type deposit. Am. Minera. 89, 1359–1366.
Pavlov, A.A., Kasting, J.F., 2002. Mass-independent fractionation of sulfur isotopes in Archean sediments: strong evidence for an anoxic Archean atmosphere. Astrobiology. 2, 27–41.
Philippot, P., van Zuilen, M., Rollion-Bard, C., 2012. Variations in atmosphere sulphur chemistry on early Erath linked to volcanic activity. Nat. Geosci. 5, 668–674.
Pi, Q.H., Hu, R.Z., Xiong, B., Li, Q.L., Zhong, R.C., 2017. In situ SIMS U-Pb dating of hydrothermal rutile, reliable age for the Zhesang Carlin-type gold deposit in the golden triangle region, SW China. Miner. Deposita. 52, 1179–1190.
Reich, M., Kesler, S.E., Utsunomiya, S., Palenik, C.S., Chryssoulis, S.L., Ewing, R.C., 2005. Solubility of gold in arsenian pyrite. Geochim. Cosmochim. Acta. 69, 2781–2796.
Ressel, M.W., Noble, D.C., Henry, C.D., Trundel, W.S., 2000. Dike-hosted ores of the Beast deposit and importance of Eocene magmatism in gold mineralization of Carlin trend. Econ. Geol. 95, 1417–1444.
Saitoh, M., Ueno, Y., Matsu'ure, F., Kawamura, T., Isozaki, Y., Yao, J.X., Ji, Z.S., Yoshida, N., 2017. Multiple sulfur isotope records at the end-Guadalupian (Permian) at Chaotian, China: implications for a role of bioturbation in the Phanerozoic sulfur cycle. J. Asian Earth Sci. 135, 70–79.
Santiago, E.S.B., Xavier, R.P., Hagemann, S.G., Monteiro, L.V.S., Cliff, J., 2021. Multiple sulfur isotopes constraints on origin and evolution of the Neoarchean and Paleoproterozoic Cu-Au systems from the Carajas Domain, Amazonian Craton, Brazil. Ore Geol. Rev. 129, 103872.
Selvaraja, V., Fiorentini, M.L., LaFlamme, C.K., Wing, B.A., Bui, T.H., 2017a. Anomalous sulfur isotopes trace volatile pathways in magmatic arcs. Geology. 45, 419–422.
Selvaraja, V., Caruso, S., Fiorentini, M.L., LaFlamme, C.K., Bui, T.H., 2017b. Atmospheric sulfur in the orogenic gold deposits of the Archean Yilgarn Craton, Australia. Geology. 45, 691–694.
Selvaraja, V., Fiorentini, M.L., Jeon, H., Savard, D.D., LaFlamme, C.K., Guagliardo, P., Caruso, S., Bui, T.H., 2017c. Evidence of local sourcing of sulfur and gold in an Archaean sediment-hosted gold deposit. Ore Geol. Rev. 89, 909–930.
Seward, T.M., 1973. Thio complexes of gold and the transport of gold in hydrothermal ore solutions. Geochim. Cosmochim. Acta. 37, 379–399.
Seward, T.M., 1991. The hydrothermal geochemistry of gold. In: Foster, R.P. (Ed.), Gold metallogeny and exploration: Glasgow. Blackie, pp. 37–62.
Simon, G., Kesler, S.E., Chryssoulis, S., 1999. Geochemistry and textures of gold-bearing arsenian pyrite, Twin Creeks, Nevada; implications for deposition of gold in Carlin-type deposit. Econ. Geol. 94, 405–421.
Smit, K.V., Shirey, S.B., Hauri, E.H., Stern, R.A., 2019. Sulfur isotopes in diamonds reveal differences in continent construction. Science 364, 383–385.
Steadman, J.A., Large, R.R., Meffre, S., Olin, P.H., Danyushevsky, L.V., Gregory, D.D., Belousov, I., Lounejeva, E., Ireland, T.R., Holden, P., 2015. Synsedimentary to early diagenetic gold in black shale-hosted pyrite nodule at the Golden Mile Deposit, Kalgoorlie, Western Australia. Econ. Geol. 110, 1157–1191.
Stefánsson, A., Seward, T.M., 2004. Gold(I) complexing in aqueous sulphide solutions to 500°C at 500 bar. Geochim. Cosmochim. Acta. 68, 4121–4143.
Su, W.C., Xia, B., Zhang, H.T., Zhang, X.C., Hu, R.Z., 2008. Visible gold in arsenian pyrite at the Shuiyindong Carlin-type gold deposit, Guizhou, China: implications for the environment and processes of ore formation. Ore Geol. Rev. 33, 667–679.
Su, W.C., Heinrich, C.A., Pettke, T., Zhang, X.C., Hu, R.Z., Xia, B., 2009a. Sediment-hosted gold deposits in Guizhou, China: products of wallrock sulfidation by deep crustal fluids. Econ. Geol. 104, 73–93.
Su, W.C., Hu, R.Z., Xia, B., Xia, Y., Liu, Y.P., 2009b. Calcite Sm-Nd isochron age of the Shuiyindong Carlin-type gold deposit, Guizhou, China. Chem. Geol. 258, 269–274.
Su, W.C., Zhang, H.T., Hu, R.Z., Ge, X., Xia, B., Chen, Y.Y., Zhu, C., 2012. Mineralogy and geochemistry of gold-bearing arsenian pyrite from the Shuiyindong Carlin-type gold deposit, Guizhou, China: implications for gold depositional processes. Miner. Deposita. 47, 653–662.
Su, W.C., Dong, W.D., Zhang, X.C., Shen, N.P., Hu, R.Z., Hofstra, A.H., Cheng, L.Z., Xia, Y., Yang, K.Y., 2018. Carlin-type gold deposits in the Dian-Qian-Gui "golden triangle" of Southwest China. Soc. Econ. Geol. 20, 157–185.

Su, W.C., 2002. The hydrothermal fluid geochemistry of the Carlin-type gold deposits in Southwestern Yangtze Craton, China. Unpublished Ph.D. dissertation, Guiyang, China, Institute of Geochemistry, Chinese Academy of Sciences (in Chinese with English abstract).

Sugiono, D., Thébaud, N., LaFlamme, C., Fiorentini, M., Martin, L., Rogers, J., Lorusso, G., McFarlane, C., 2021. Integration of multiple sulfur isotopes with structural analysis unveils the evolution of ore fluids and source of sulfur at the Kanowna Belle Archean orogenic gold deposit, Yilgarn Craton, Western Australia. Miner. Deposita. 56, 1471–1490.

Suo, S.T., Bi, X.M., Zhao, W.X., Hou, G.J., 1998. Very low-grade metamorphism and its geodynamical significance of Triassic strata within the Youjiang River basin. Sci. Geol. Sin. 33, 396–405 (in Chinese with English abstract).

Wang, F.Y., Ge, C., Ning, S.Y., Nie, L.Q., Zhong, G.X., White, N.C., 2017. A new approach to LA-ICP-MS mapping and application in geology. Acta Petrol. Sin. 33, 3422–3436 (in Chinese with English abstract).

Wei, D.T., Xia, Y., Gregory, D.D., Steadman, J.A., Tan, Q.P., Xie, Z.J., Liu, X.J., 2020. Multistage pyrites in the Nibao disseminated gold deposit, southwestern Guizhou Province, China Insights into the origin of Au from textures, in situ trace elements, and sulfur isotope analyses. Ore Geol. Rev. 122, 103446.

Wilson, S.A., Ridley, W.I., Koenig, A.E., 2002. Development of sulfide calibration standards for the laser ablation inductively-coupled plasma mass spectrometry technique. J. Anal. At. Spectrom. 17, 406–409.

Wu, W., 2018. Mineralization of the Jinya and Nakuang Carlin-like gold deposits in Northwest Guangxi. M.D. Thesis, China University of Geosciences (Beijing), Beijing, China (in Chinese with English abs).

Xie, Z.J., Xia, Y., Cline, J.S., Koenig, A., Wei, D.T., Tan, Q.P., Wang, Z.P., 2018a. Are there Carlin-type gold deposits in China? A comparison of the Guizhou, China, deposits with Nevada, USA, deposits. Soc. Econ. Geol. 20, 187–233.

Xie, Z.J., Xia, Y., Cline, J.S., Pribil, M.J., Koenig, A., Tan, Q.P., Wei, D.T., Wang, Z.P., Yan, J., 2018b. Magmatic origin for sediment-hosted Au deposits, Guizhou Province, China: in situ chemistry and sulfur isotope composition of pyrites, Shuiyindong and Jinfeng deposits. Econ. Geol. 113, 1627–1652.

Xue, Y.X., Campbell, I., Ireland, T.R., Holden, P., Armstrong, R., 2013. No mass-independent sulfur isotope fractionation in auriferous fluids supports a magmatic origin for Archean gold deposits. Geology. 41, 791–794.

Yan, J., Hu, R.Z., Liu, S., Lin, Y.T., Zhang, J.C., Fu, S.L., 2018. NanoSIMS element mapping and sulfur isotope analysis of Au-bearing pyrite from Lannigou Carlin-type Au deposit in SW China: new insights into the origin and evolution of Au-bearing fluids. Ore Geol. Rev. 92, 29–41.

Yan, D.P., Zhou, M.F., Wang, Y.C., Xia, B., 2006. Structural and geochronological constraints on the tectonic evolution of the Dulong-Song Chay tectonic dome in Yunnan Province, SW China. J. Asian Earth Sci. 28, 332–353.

Yang, J.H., Cawood, P.A., Du, Y.S., Huang, H., Hu, L.S., 2012. Detrital record of Indosinian mountain building in SW China: provenance of the Middle Triassic turbidites in the Youjiang basin. Tectonophysics. 574–575, 105–117.

Yang, L., Deng, J., Groves, D.I., Wang, Q.F., Zhang, L., Wu, W., Qin, K., Zhang, Q.Z., 2020. Recognition of two contrasting structural- and mineralogical-gold mineral systems in the Youjiang basin, China-Vietnam: orogenic gold in the south and Carlin-type in the north. Geosci. Front. 111, 1477–1494.

Zaw, K., Meffre, S., Lai, C.K., Burrett, C., Santosh, M., Graham, I., Manaka, T., Salam, A., Kamvong, T., Cromie, P., 2014. Tectonic and metallogeny of mainland Southeast Asia: a review and contribution. Gondwana Res. 26, 5–30.

Zhang, G.J., Zhang, X.L., Li, D.D., Farquhar, J., Shen, S.Z., Chen, X.Y., Shen, Y., 2015. Widespread shoaling of sulfidic waters linked to the end-Guadalupian (Permian) mass extinction. Geology. 43, 1091–1094.

Zhao, J., Liang, J.L., Li, J., Huang, Y., Liu, X., Zhang, J.C., Hao, J.L., Sun, W.D., Li, J.Z., Xie, J.Q., 2020. Gold and sulfur sources of the Taipingdong Carlin-type gold deposit: constraints from simultaneous determination of sulfur isotopes and trace elements in pyrite using nanoscale secondary ion mass spectroscopy. Ore Geol. Rev. 117, 103299.

Zhu, J.J., Hu, R.Z., Richards, J.P., Bi, X.W., Stern, R., Lu, G., 2017. No genetic link between Late Cretaceous felsic dikes and Carlin-type Au deposits in the Youjiang basin, Southwest China. Ore Geol. Rev. 84, 328–337.

Zhu, J., Zhang, Z.C., Santosh, M., Jin, Z.L., 2019. Carlin-style gold province linked to the extinct Emeishan plume. Earth Planet. Sci. Lett. 530, 115940.